IDEA League

Master of Science in Applied Geophysics

Research Thesis

Joint inversion of shear-wave velocity azimuthal anisotropy from surface and body waves

Julian Kühnert

August 12, 2016

Joint inversion of shear-wave velocity azimuthal anisotropy from surface and body waves

Master of Science Thesis

for the degree of Master of Science in Applied Geophysics at
Delft University of Technology
ETH Zürich
RWTH Aachen University
by

Julian Kühnert

August 12, 2016

Department of Geoscience & Engineering · Delft University of Technology
Department of Earth Sciences · ETH Zürich
Faculty of Georesources and Material Engineering · RWTH Aachen University

Copyright © 2016 by IDEA League Joint Master's in Applied Geophysics:

ETH Zürich

All rights reserved.
No part of the material protected by this copyright notice may be reproduced or utilized in any form or by any means, electronic or mechanical, including photocopying or by any information storage and retrieval system, without permission from this publisher.

Printed in Switzerland

IDEA LEAGUE
JOINT MASTER'S IN APPLIED GEOPHYSICS

Delft University of Technology, The Netherlands
ETH Zürich, Switzerland
RWTH Aachen, Germany

Dated: *August 12, 2016*

Supervisor(s):

Dr. Daniele Boiero (Schlumberger)

Dr. Claudio Bagaini (Schlumberger)

Dr. Edgar Manukyan (ETH Zürich)

Committee Members:

Dr. Claudio Bagaini (Schlumberger)

Dr. Edgar Manukyan (ETH Zürich)

Dr. Ranajit Ghose (TU Delft)

Abstract

The phenomenon of shear-wave splitting (SWS), in which the shear-wave (S-wave) splits into a fast traveling and a slow traveling component of different polarization, is the key indicator for shear-wave velocity anisotropy. Despite conveying valuable subsurface information, the phenomenon potentially degrades the seismic image quality. For these reasons, after being investigated predominantly in fields of global seismology, the analysis and compensation of SWS forms now a routine step for S-wave processing in reflection seismology. When a S-wave source is not available, the orientation of the fast and the slow axis of the anisotropic medium and the magnitude of the velocity variation can be determined by analyzing the azimuthal variations of reflection events from compressional- to shear-wave (PS-) converted waves. However, PS-waves can not be consulted for anisotropy information in the near-surface due to low coverage and contamination from coherent noise. Here, surface waves can provide the missing information by analyzing the azimuthally varying phase velocities.
As the body waves and the surface waves are sensitive to the same anisotropic properties, their data can elegantly be combined and inverted. The performance of the inversion with combined data in determining the subsurface anisotropic properties is superior to a sole body wave inversion due to the complementarity of the to wave types. This is highlighted when using the inversion results for the compensation of the effect of SWS. Through the incorporation of the surface waves, the near surface can be compensated correctly which consequently leads to an enhanced compensation beneath.

Acknowledgments

First of all I want to thank my principal supervisor Daniele Boiero at Schlumberger for his guidance and his ever open ear to any kind of query. He supplied me with the right amount of input and encouraged me in my own ideas. Beyond the technical aspect he definitely did his bit to give me an enjoyable and fun time in the Schlumberger House.

Further, I want to acknowledge my second supervisor Claudio Bagaini at Schlumberger. His detailed questionings let me achieve further progress. Due to the regular meetings with Daniele I certainly received more input from him than I can appreciate.

Generally, I want to thank the whole team at Schlumberger in Gatwick for the possibility to carry out my thesis project in the company and thereby letting me have rich and pleasant 5 and a half months. Further, thanks to Schlumberger to provide the seismic modeling codes which were used for this thesis.

A big thanks goes to my academic supervisor Edgar Manukyan at the ETH Zurich. I did not experience a single exchange with him which was not constructive. Regardless of all time constraints and Visa obstacles, he made the effort to take a flight and visit me in Gatwick for one afternoon. Needless to say that this afternoon ended highly constructive.

I also want to thank Jean-Paul Montagner at IPGP, one of the leading researchers in the studied field. In a spontaneous encounter he willingly discussed on some details of one of his papers and offered me his help and support.

Additionally, I want to acknowledge the scholarship I receive from E.ON within the German student funding program 'Bildungsfond', which has been supporting me for my Master's study.

Finally, many thanks to my classmates and London flatmates Erik and Fabian, with whom I went together through the whole Schlumberger experience, to my family, who indeed made my studies up to this point possible, and to Gabriela, who, besides all other unutterable support, encouraged me to carry out the IDEA League Joint Master's program.

Swiss Federal Institute of Technology — Julian Kühnert
August 12, 2016

Table of Contents

Abstract v

Acknowledgments vii

Acronyms xvii

1 Introduction 1
- 1-1 Seismic anisotropy and shear-wave splitting . . . 1
- 1-2 The estimation of shear-wave velocity anisotropy . . . 3

2 Shear-wave velocity anisotropy from body and surface waves 5
- 2-1 Elastic moduli and shear-wave velocity anisotropy . . . 5
- 2-2 Body wave anisotropy - shear-wave splitting and splitting intensity . . . 8
- 2-3 Surface wave anisotropy - phase velocity azimuthal variation . . . 9
- 2-4 Merging the systems of surface and body waves . . . 10

3 Data analysis and inversion: method 11
- 3-1 Preparation of 1D-model and synthetic seismogram . . . 11
- 3-2 Splitting intensity measurement . . . 14
- 3-3 Surface wave phase velocity measurement . . . 16
- 3-4 Sensitivities and inversion . . . 18
  - 3-4-1 Sensitivity kernels . . . 18
  - 3-4-2 Normalization of the sensitivity kernels . . . 18
  - 3-4-3 Inversion algorithm . . . 19

4 1D-model: inversion results and shear-wave splitting compensation 21
- 4-1 Body wave inversion . . . 21
- 4-2 Surface wave inversion . . . 23
- 4-3 Joint inversion . . . 24
- 4-4 Shear-wave splitting compensation . . . 27

5 3D-model: set-up and inversion **31**
5-1 Set-up of the 3D-model 31
5-2 Synthetic seismogram and data acquisition 34
5-3 Body wave inversion 35
5-4 Surface wave inversion 37
5-5 Results joint inversion 39

6 Conclusion and Outlook **43**
6-1 Summary and conclusion 43
6-2 Outlook 44

A Parameters and further results **49**
A-1 1D-model: Set-up parametrization 49
A-2 3D-model: Results joint inversion 50

List of Figures

1-1 *Left:* Ray path in a simple source-receiver geometry. The arrows indicate the particle motions of P-wave (purple) and S-wave (olive). After PS-conversion, the S-wave polarization lays within the radial plane of propagation (blue). *Right:* Illustration of shear-wave splitting (SWS). The upcoming S-wave with radial polarization (blue) encounters an anisotropic layer and splits into a component with polarization parallel to the fast axis (red) and one with polarization parallel to the slow axis (green). Due to the different velocities, a time delay δt builds up between the two components. Axis annotations indicate beside the commonly used x-, y-, z-axis, the geographic coordinates (**N** (North), **E** (East)), the wave propagation coordinates (R (Radial), T (Transverse)), and the anisotropic coordinates (f (fast axis), s (slow axis)). 2

2-1 *Left*: Definition of the 9 independent elastic coefficients of a orthorhombic material. *Right*: HTI symmetry with x as the rotational symmetry axis. 6

2-2 The systems of geographic coordinates (**N** (North), **E** (East)), anisotropic coordinates (f (fast axis), s (slow axis)), and the wave propagation coordinates (R (Radial), T (Transverse)). The angles Ψ_f and Ψ define fast axis direction and azimuth of R, respectively. 7

3-1 1D-model depth parameter: P-wave velocities v_x, v_y, v_z (*left*), S-wave velocities v_{yz}, v_{xz}, v_{xy} (*middle*) and density ρ (*right*). 12

3-2 1D-model depth parameter: *Thomsen* parameter γ (*left*) and fast axis direction Ψ_f (*right*). 12

3-3 Synthetic seismogram of the 1D model (*left*): xz-plane slice of x-component PS-primaries response.Bandwidth ranges from 0.5 Hz to 40.0 Hz. *2 graphs on the right*: Radial and transverse component as functions of azimuth extracted form an offset range from 240 m to 260 m (illustrated by the green lines on the left graph). Red boxes mark the reflection events SI1 to SI5 for the SI-measurements. 13

3-4 Synthetic seismogram of the 1D model: xz-plane slice of z-component full response. Bandwidth ranges from 0.5 Hz to 10.0 Hz. This data will be used for the surface wave analysis. 14

3-5 Extraction of data from a receiver grid (gray dots, 10 m spacing) within different azimuth sections: the gray ring illustrates the offset range of 240-260 m (*left*, the red star denotes the source). Radial component (*middle*) and transverse component (*right*) of the data after sorting by azimuth (the red lines correspond to the illuminated sector in the left graph). 15

3-6 Splitting intensity SI-measurements for the reflection events SI1 and SI5. Asterisks denote the measurement picks, the solid lines are the π-periodic fits. 15

3-7 Illustration of the extraction process of the surface wave data (within the gray shaded disk of 2000 m radius) from a receiver grid (gray dots, 10 m spacing) in azimuths sections of 6° width (*left*, the red star denotes the source). Stacked data of frequency 6 Hz in the $k\Psi$-domain (*middle*, with the red lines corresponding to the illuminated sector in the left graph) and stacked data at azimuth $36° \pm 3°$ in the fk-domain (*right*). Overlaid the expected location of the 1st mode (dashed, purple). 16

3-8 The azimuthal variation of the phase velocity v_R for frequencies 2 Hz and 8 Hz. Asterisks denote the measured values, calculated from the fk-pairs, the solid lines correspond to the π-periodic sinusoidal fits. 17

3-9 The wavenumber variation as a function of azimuth at surface wave frequencies 4 Hz (*left*) and 8 Hz (*right*). We can observe that the lower frequency signal is related to a smaller wavenumber and smaller wavenumber variation. 17

3-10 Layer sensitivities of surface waves dependent on their frequency (*left*) and of body waves for the different reflection events SI1 to SI5 (*right*). 18

3-11 Sum of sensitivities over each layer for the cosine-system (*left*) and the sine-system (*right*) to compare the different normalization approaches: Data normalization (red) and RMS normalization (yellow). Note the logarithmic scale of the sensitivities. 19

4-1 *2 graphs on the left:* Comparison between measured and predicted data coefficients b_C and b_S. The measured data contain error bars. *2 graphs on the right:* Comparison between inversion results and true model parameter for the anisotropic coefficients G_C and G_S. 22

4-2 *Left*: Layered anisotropic velocity from inversion (solid lines) compared with the true model velocity (dashed lines). Relative shear-wave anisotropy G/L (*middle*) and fast axis direction Ψ_f (*right*) from true model and inversion results. 22

4-3 *2 graphs on the left:* Comparison between measured and predicted data coefficients a_C and a_S. The measured data contain error bars. *2 graphs on the right:* Comparison between inversion results and true model parameter for the anisotropic coefficients G_C and G_S. 23

4-4 *Left*: Layered anisotropic velocity from inversion (solid lines) compared with the true model velocity (dashed lines). Relative shear-wave anisotropy G/L (*middle*) and fast axis direction Ψ_f (*right*) from true model and inversion results. 24

4-5 *2 graphs on the left:* Comparison between measured and predicted data coefficients a_C, a_S and b_C, b_S. The measured data contain error bars. *2 graphs on the right:* Comparison between inversion results and true model parameter for the anisotropic coefficients G_C and G_S. 25

4-6 *Left*: Layered anisotropic velocity from inversion (solid lines) compared with the true model velocity (dashed lines). Relative shear-wave anisotropy G/L (*middle*) and fast axis direction Ψ_f (*right*) from true model and inversion results. 26

4-7 Azimuthally varying PS-signals on radial (R) and transverse (T) component: uncorrected (*2 graphs on the l.h.s.*) and corrected using the results of the body-wave inversion (PS, *2 graphs on the r.h.s.*). 27

4-8 Azimuthally varying PS-signals on radial (R) and transverse (T) component: corrected using the results of the body-wave inversion (PS, *2 graphs on the l.h.s.*) and corrected using the results of the joint inversion (joint, *2 graphs on the r.h.s.*). 28

4-9 Azimuthally varying PS-signals on radial (R) and transverse (T) component: corrected using the results of the joint inversion (joint, *2 graphs on the l.h.s.*) and corrected using the theoretical SWS-values (true, *2 graphs on the r.h.s.*). 29

5-1 S-wave velocity v_{sv} distribution within two orthogonal depth slices in the x-plane (*left*) and the y-plane (*right*). The red lines define the shallow horizons H1 to H4 with constant depth from 100 m to 400 m and the deeper horizons H5 to H7. Note that H7 corresponds to the top of the reservoir. 32

5-2 Density ρ distribution within two orthogonal depth slices (similar as in Figure 5-1). The red lines mark horizons H1 to H7. 32

5-3 Magnitude of anisotropy, denoted by Thomsen parameter γ, within two orthogonal depth slices (similar as in Figure 5-1). The red lines mark horizons H1 to H7. . . 33

5-4 Fast axis direction Ψ_f (red lines) in the defined blocks down H4 (top left), H5 (top right), H6 (bottom left), and H7 (bottom right). The background shows the average S-wave velocity of the corresponding zone. 33

5-5 x-component (*left*) and y-component (*center*) of the modeled data from the 3D-model (seimograms show y-slices at $x = 0$ m). *Right:* The corresponding section of the modeled data from the 1D-model. 34

5-6 Relative anisotropy G/L (background) and fast axes direction Ψ_f (red lines) of the true model (*left column*) and from the body wave inversion (*right column*) for the 4 deepest overburden layers betweens horizons H3-H4, H4-H5, H5-H6, and H6-H7. 36

5-8 *Left:* S-wave velocity distribution and fast axes direction. *Right:* Inversion results (anisotropy magnitude and orientation) for the same region. 37

5-7 Relative anisotropy G/L (background) and fast axes direction Ψ_f (red lines) of the true model (*left column*) and from the surface wave inversion (*right column*) for the 4 shallow layer down to horizon H4. 38

5-9 Relative anisotropy G/L (background) and fast axes direction Ψ_f (red lines) of the true model (*top left*) and from the body wave (PS-) inversion (*top right*), the joint inversion with measured surface wave data (*bottom left*) and the joint inversion with synthetic surface wave data (*top right*) for layer between horizons H4 and H5. 39

5-10 Relative anisotropy G/L (background) and fast axes direction Ψ_f (red lines) of the true model (*top left*) and from the body wave (PS-) inversion (*top right*), the joint inversion with measured surface wave data (*bottom left*) and the joint inversion with synthetic surface wave data (*top right*) for layer between horizons H3 and H4. 40

5-11 Relative anisotropy G/L (background) and fast axes direction Ψ_f (red lines) from the surface wave inversion (*left*) and, from the same surface wave data, the joint inversion (*right*) for layer between horizons H3 and H4. 41

A-1 Relative anisotropy G/L (background) and fast axes direction Ψ_f (red lines) of the true model (*top left*) and from the body wave (PS-) inversion (*top right*), the joint inversion with measured surface wave data (*bottom left*) and the joint inversion with synthetic surface wave data (*top right*) for layer between horizons H6 - H7 (*top half*) and H6 - H7 (*bottom half*). 51

List of Tables

A-1 Set-up parameters for the 1D-model: Layer number, layer thickness d, background P-wave velocity v_p, background S-wave velocity v_s, density ρ, and dimensionless *Thomsen* parameters ϵ, γ, and δ. 50

Acronyms

HTI horizontal transverse isotropic

PS P-wave to S-wave converted waves

SWS shear-wave splitting

SI splitting intensity

TWT two-way travel time

Chapter 1

Introduction

The present thesis is studying the phenomenon of shear-wave azimuthal anisotropy and its effect on seismic imaging. The work is meant to contribute to the quantification of anisotropic elastic properties in reflection seismology by presenting a novel approach to jointly invert body shear wave and surface wave data.

1-1 Seismic anisotropy and shear-wave splitting

It was not until the 1980s, after the review paper on wave motion in anisotropic and cracked elastic-media of Crampin (1981) and the first International Workshop on Seismic Anisotropy in 1982, that the phenomenon of seismic anisotropy in the Earth's crust was universally accepted (Crampin and Gao, 2009). Since then, the understanding of seismic wave propagation in anisotropic media has widely advanced and forms nowadays an integral component in global seismology as well as in engineering and exploration geophysics.
Isotropy (from the Greek: *isos* 'equal', *tropos* 'way' (Wikipedia, 2016)) describes the property of being uniform in all directions. Anisotropy is hence the directional inequality. Seismic waves traveling in an anisotropic subsurface experience different medium properties dependent on their direction of propagation or their polarization.
Body shear waves (S-waves) are characterized by their polarization. In reflection seismology they can be referred to S_V-waves and S_H-waves when polarized in the vertical plane and in the horizontal plane, respectively. In a simple source-receiver geometry as shown in Figure 1-1, where S-waves are created from P-waves due to mode conversion at interfaces (P-wave to S-wave converted waves (PS)), only S_V-waves polarized in the radial (source-receiver) direction are expected at the receiver. However, in case of an anisotropic medium, S_H-waves can be created and recorded as transverse component.
Let's assume nearly vertically traveling S_V-waves and a medium characterized by azimuthal anisotropy (horizontal transverse isotropic (HTI), see Section 2-1). The polarization of the S_V-waves can be aligned either with the so-called fast axis of the medium or, perpendicular to it, the slow axis of the medium. A polarization in between the two principal directions

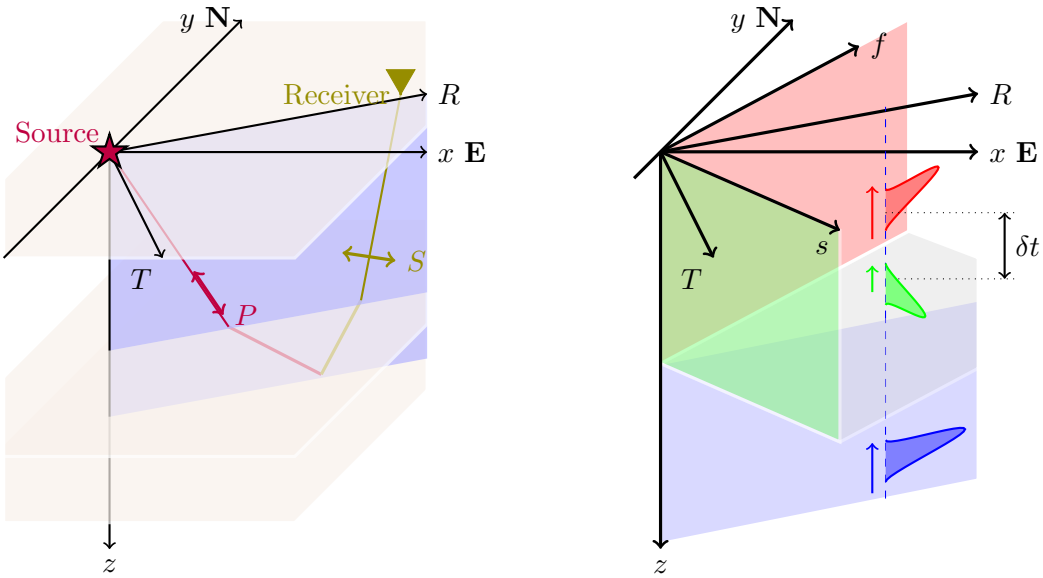

Figure 1-1: *Left:* Ray path in a simple source-receiver geometry. The arrows indicate the particle motions of P-wave (purple) and S-wave (olive). After PS-conversion, the S-wave polarization lays within the radial plane of propagation (blue). *Right:* Illustration of shear-wave splitting (SWS). The upcoming S-wave with radial polarization (blue) encounters an anisotropic layer and splits into a component with polarization parallel to the fast axis (red) and one with polarization parallel to the slow axis (green). Due to the different velocities, a time delay δt builds up between the two components. Axis annotations indicate beside the commonly used x-, y-, z-axis, the geographic coordinates (**N** (North), **E** (East)), the wave propagation coordinates (R (Radial), T (Transverse)), and the anisotropic coordinates (f (fast axis), s (slow axis)).

will cause the wave to split into a fast-traveling and a slow-traveling signal. Figure 1-1 shows this scenario on the right hand side. In this case, a transverse component and varying arrival times can be measured at the receiver. If multiple layers of different fast axis directions are encountered on the way to the surface, the signals will split multiple times in sets of fast and slow traveling components. This phenomenon is commonly known as shear-wave splitting shear-wave splitting (SWS) or seismic birefringence and is somewhat of an double-edged sword for following reasons:

- **Image deterioration**
  The interference of split signals traveling at different velocities and building up phase shifts can degrade the seismic image quality to a great extent. To regain resolution for example for reservoir mapping, the effect of SWS must be corrected for. This can be a complex task in case of the presence of multiple anisotropic layers.

- **Rock characterization**
  Rock mineralogy, fractures or other internal structures of the rock and the orientation of surrounding stress fields are potential causes for anisotropy (Crampin et al., 1984). As S-waves are highly sensitive to rock anisotropy, SWS is a paramount tool to provide insight to rock properties and subsurface structures. To emphasize its potential, Crampin (2006) sees SWS as the key phenomenon to observe stress-aligned fluid satu-

rated microcracks, which potentially trigger rock fracturing when gathered in so called critical systems. He calls out for the need of a *New Geophysics*, in which SWS is used to *monitor* deformation of the crust. The observed stress changes can then be evaluated to *calculate* the evaluation and *predict* future behavior of the subsurface. This can be of high value for example in hazard detection and prevention or in (unconventional) hydrocarbon exploration.

1-2 The estimation of shear-wave velocity anisotropy

SWS estimation is crucial for both image enhancement and rock characterization. But how can the magnitude and the orientation of the anisotropy be determined?
Conventionally, to correct for SWS in the seismic image, a so called layer stripping procedure is applied. In this approach, the splitting parameters such as the time delay between fast and slow signal and their azimuthal orientations are estimated and corrected layer by layer downwards to increasing reflection times. Chevrot (2000) introduces the splitting intensity (SI) as a measure of SWS. This property can be linearly related to anisotropic perturbation at depth by summing along the wave path and allows to invert directly to the subsurface anisotropic elastic properties as will be shown later.
However, poor S-wave coverage in shallow layers cause uncertainties on both the layer stripping approach and the SI inversion so that the anisotropy estimation is biased for deeper layers. Surface waves have good potential to resolve this problem providing missing near surface data.
The present study takes advantage of the fact that S-waves and surface waves are sensitive to the same subsurface properties and shows how they complement each other by jointly inverting them for anisotropic elastic coefficients which are used to determine shear-wave velocity anisotropy.

Chapter 2

Shear-wave velocity anisotropy from body and surface waves

This chapter covers the fundamental description of an elastic anisotropic medium with a horizontal symmetry axis and the propagation of shear waves and surface waves in such a medium.

2-1 Elastic moduli and shear-wave velocity anisotropy

To characterize the propagation of seismic waves in an anisotropic medium, a detailed description of the elastic moduli is needed. Fundamental to this is the generalized Hooke's Law which relates stress vector $\vec{\sigma}$ to strain vector $\vec{\varepsilon}$ via the elastic modulus matrix C:

$$\vec{\sigma} = C\vec{\varepsilon}. \tag{2-1}$$

The so-called stiffness matrix C contains 21 independent elastic coefficients for most general anisotropic materials (e.g. Rand and Rovenski (2007)). The number of independent coefficients reduces to 9 for materials with three orthogonal planes of symmetry, which are referred to as orthorhombic materials. The left hand side of Figure 2-1 defines those 9 independent coefficients.
Of particular relevance in the context of azimuthal anisotropy are transversely isotropic (or hexagonal) materials. These materials contain an axis of rotational symmetry and can be characterized by 5 independent coefficients. In the following we will especially deal with a horizontal transverse isotropic (HTI) medium as for example a subsurface containing parallel vertical fracture planes would be classified as. The symmetry of the HTI can be seen on the

right hand side of Figure 2-1. The stiffness matrix for a HTI becomes:

$$C = \left(\begin{array}{ccc|ccc} C_{11} & C_{13} & C_{13} & 0 & 0 & 0 \\ C_{13} & C_{33} & C_{33}-2C_{44} & 0 & 0 & 0 \\ C_{13} & C_{33}-2C_{44} & C_{33} & 0 & 0 & 0 \\ \hline 0 & 0 & 0 & C_{44} & 0 & 0 \\ 0 & 0 & 0 & 0 & C_{66} & 0 \\ 0 & 0 & 0 & 0 & 0 & C_{66} \end{array}\right) \tag{2-2}$$

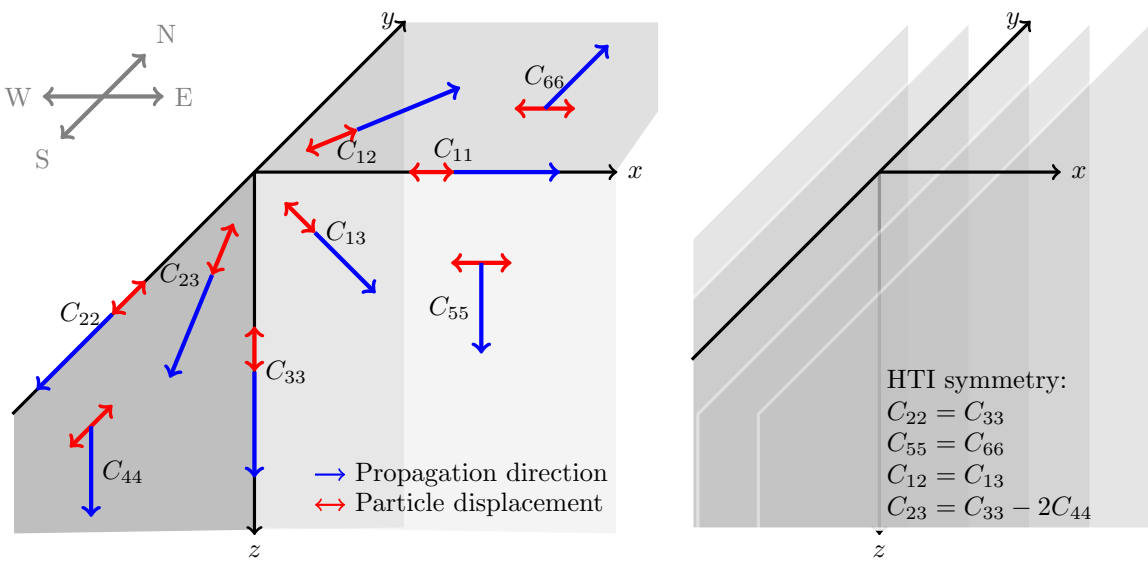

Figure 2-1: *Left*: Definition of the 9 independent elastic coefficients of a orthorhombic material. *Right*: HTI symmetry with x as the rotational symmetry axis.

The elastic coefficients of the stiffness matrix C are directly related to the seismic velocities. The P-wave velocities v_{pi} along the main axes $i = x, y, z$ and the S-wave velocities v_{sj} in the planes $j = yz, xz, xy$ relate to the coefficients on the main diagonal of the stiffness matrix:

$$\begin{aligned} C_{11} &= \rho v_{px}^2, & C_{22} &= \rho v_{py}^2, & C_{33} &= \rho v_{pz}^2, \\ C_{44} &= \rho v_{syz}^2, & C_{55} &= \rho v_{sxz}^2, & C_{66} &= \rho v_{sxy}^2. \end{aligned} \tag{2-3}$$

where ρ denotes the density of the material. Vertically traveling body shear waves are governed by the elastic moduli C_{44} and $C_{55}(= C_{66}$ for HTI) as can be easily seen from Figure 2-1 (left). Likewise, vertically polarized surface waves are controlled by the same parameters, which can be comprehended when the vectors in Figure 2-1 are rotated in their corresponding plane. Thus, the combination of those two parameters is key to deduce the azimuthal shear-wave velocity anisotropy. The constant or isotropic (i.e. azimuthally independent) component is the average over C_{44} and C_{55} and is commonly defined as L (e.g. Montagner and Nataf (1986)). L corresponds therefore to the average velocity which I will denote as $\bar{v}_{sv}$ corresponding to both vertically traveling body shear waves and vertically polarized surface waves:

$$L := \frac{1}{2}(C_{44} + C_{55}) = \frac{1}{2}\rho(v_{sx}^2 + v_{sy}^2) = \rho\bar{v}_{sv}^2. \tag{2-4}$$

The anisotropic part is in its simplest form composed of the difference of C_{44} and C_{55} and variates azimuthally with π-periodicity. Taking the azimuth Ψ from the North the azimuthal variation is: $\frac{1}{2}(C_{44} - C_{55}) \cos 2\Psi$ (note that the here used left-handed coordinate system is taken into account).

In the more general case, the fast axis direction Ψ_f does not point towards the North. That is, in the words of Montagner et al. (2000), the geographic coordinate system does not coincide with the anisotropic coordinate system. Figure 2-2 illustrates the constellation of the different coordinate systems and defines the corresponding angles of azimuth.

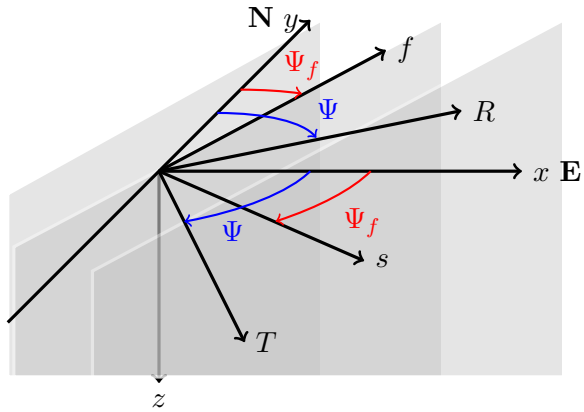

Figure 2-2: The systems of geographic coordinates (**N** (North), **E** (East)), anisotropic coordinates (f (fast axis), s (slow axis)), and the wave propagation coordinates (R (Radial), T (Transverse)). The angles Ψ_f and Ψ define fast axis direction and azimuth of R, respectively.

In order to measure the anisotropy experienced by the propagating waves in the radial plane with angle Ψ in respect to the North, the stiffness matrix has to be rotated from the anisotropic coordinate system into the geographic coordinate system which causes an additional term C_{45} to appear. The azimuthal velocity variation becomes

$$\rho v_{sv}^2 = \frac{1}{2}(C_{44} + C_{55}) + \frac{1}{2}(C_{44} - C_{55}) \cos 2\Psi + C_{45} \sin 2\Psi. \tag{2-5}$$

Following the notation of Montagner and Nataf (1986), we define the anisotropic parameters $G_C = (C_{44} - C_{55})/2$ and $G_S = C_{45}$ and rewrite the expression as

$$\rho v_{sv}^2 = L + G_C \cos 2\Psi + G_S \sin 2\Psi. \tag{2-6}$$

The anisotropic variations G_C and G_S are typically much smaller than the constant term L, which is why the azimuthal S-wave velocity can be approximated in a first-order expansion:

$$\begin{aligned} v_{sv} &= \sqrt{\frac{L + G_C \cos 2\Psi + G_S \sin 2\Psi}{\rho}} \\ &\overset{(L \gg G_C, G_S)}{\approx} \sqrt{\frac{L}{\rho}} \left(1 + \frac{G_C}{2L} \cos 2\Psi + \frac{G_S}{2L} \sin 2\Psi\right) \\ &= \bar{v}_{sv} \left(1 + \frac{G}{2L} \cos 2(\Psi - \Psi_f)\right), \end{aligned} \tag{2-7}$$

with $G = \sqrt{G_C^2 + G_S^2}$ and the fast axis direction $\Psi_f = 0.5 \tan^{-1}(G_S/G_C)$. Further, the relative velocity variation $\delta v_{sv}/\bar{v}_{sv}$ can be derived, noting that the slow axis direction corresponds to $\Psi_s = \Psi_f + \pi/2$ (Montagner et al., 2000):

$$\frac{\delta v_{sv}}{\bar{v}_{sv}} = \frac{v_{sv}(\Psi_f) - v_{sv}(\Psi_s)}{\bar{v}_{sv}} = \frac{G}{L}. \tag{2-8}$$

As already indicated, the medium parameter L and its azimuthal variations G_C and G_S govern the anisotropic behavior of both the body waves and the the surface waves. The next 2 sections derive the relations between these medium parameters and the observed phenomena, namely shear-wave splitting in case of body waves and azimuthal varying phase velocities in case of surface waves.

2-2 Body wave anisotropy - shear-wave splitting and splitting intensity

Body shear waves propagating vertically through a HTI undergo a so called shear-wave splitting. Depending on the polarization, the shear-wave will split into a component parallel and perpendicular to the fast axis, in between which a phase difference and a time delay will build up. Taking the relative velocity variation from Eq. (2-8), the delay time δt_i between fast and slow wave within a layer i from depth z_i to depth z_{i-1} in a weak isotropic medium can be expressed as (Montagner et al., 2000)

$$\delta t_i = \frac{(z_i - z_{i-1})\,\delta v_{sv_i}}{\bar{v}_{sv_i}^2} = \frac{\delta z_i}{\bar{v}_{sv_i}}\frac{G_i}{L_i} = \sqrt{\frac{\rho_i}{L_i}}\frac{\delta z_i}{L_i}G_i. \tag{2-9}$$

The shear-wave will split multiple times if it passes multiple anisotropic layers of different fast axis directions. By summing up Eq. (2-9) over n layers, the total delay time $\delta\bar{t}$ and the effective fast axis direction $\bar{\beta}$ become

$$\delta\bar{t}\,\sin 2\bar{\beta} = \sum_{i=1}^{n} \delta t_i \sin 2\beta_i, \tag{2-10}$$

where $\bar{\beta} = \bar{\Psi}_f - \Psi$ with the fast axis direction $\bar{\Psi}_f$ and the ray path direction Ψ from the North. For each layer applies $\beta_i = \Psi - \Psi_{f_i}$. Combining Eq. (2-9) and Eq. (2-10) yields

$$\begin{aligned}
\delta\bar{t}\,\sin 2\bar{\beta} &= \sin 2\Psi \sum_{i=1}^{n} \frac{\delta z_i}{\bar{v}_{sv_i}}\frac{G_i \cos 2\Psi_{f_i}}{L_i} - \cos 2\Psi \sum_{i=1}^{n} \frac{\delta z_i}{\bar{v}_{sv_i}}\frac{G_i \sin 2\Psi_{f_i}}{L_i} \\
&=: \sin 2\Psi \underbrace{\sum_{i=1}^{n} \frac{\delta z_i}{\bar{v}_{sv_i}}\frac{G_{C_i}}{L_i}}_{=:b_C} - \cos 2\Psi \underbrace{\sum_{i=1}^{n} \frac{\delta z_i}{\bar{v}_{sv_i}}\frac{G_{S_i}}{L_i}}_{=:-b_S} \\
&= b_C\,\sin 2\Psi + b_S\,\cos 2\Psi = \delta\bar{t}\sin 2(\Psi - \bar{\Psi}_f).
\end{aligned} \tag{2-11}$$

Thus, $\delta\bar{t} = \sqrt{b_C^2 + b_S^2}$ and $\bar{\Psi}_f = 0.5\tan^{-1}(b_C/b_S)$. The azimuthally varying delay time has been defined by Chevrot (2000) as splitting intensity SI: $SI(\Psi) := \delta\bar{t}\,\sin 2\bar{\beta}$. With Eq. (2-11) on hand we can now describe the data in terms of splitting intensity and relate it to the earth properties. For this, the data is sorted into radial and transverse components and the delay times of specified reflection events are picked and fitted to obtain the parameters b_C and b_S. In the inversion routine, the parameters of all events are collected in the data vector while

the layer specific G_{C_i} and G_{S_i} form the model vector. Written in matrix-vector form

$$\begin{pmatrix} b_{C_1} \\ \vdots \\ b_{C_k} \\ \vdots \\ b_{C_M} \end{pmatrix} = \left[\sqrt{\frac{\rho}{L}}\frac{\delta z}{L}\right]_{ki} \begin{pmatrix} G_{C_1} \\ \vdots \\ G_{C_i} \\ \vdots \\ G_{C_K} \end{pmatrix}, \quad \begin{pmatrix} b_{S_1} \\ \vdots \\ b_{S_k} \\ \vdots \\ b_{S_M} \end{pmatrix} = -\left[\sqrt{\frac{\rho}{L}}\frac{\delta z}{L}\right]_{ki} \begin{pmatrix} G_{S_1} \\ \vdots \\ G_{S_i} \\ \vdots \\ G_{S_K} \end{pmatrix}, \tag{2-12}$$

for all reflection events $k = 1, ..., M$ and all layers $i = 1, ..., K$. The elements of the matrices are referred to as sensitivity kernels. In this work it is assumed, that an isotropic velocity model already exists. The sensitivities can thus be calculated and only the anisotropic parameters are inverted for.

2-3 Surface wave anisotropy - phase velocity azimuthal variation

In the following the theoretical framework for the description of azimuthal varying velocity of surface waves is constructed. Surface waves, sometimes also called interface waves, travel along the interfaces formed by vacuum-solid, liquid-solid or solid-solid. Their penetration depth is proportional to the wavelength and their velocity is mainly dependent on the corresponding S-wave velocity.
Following the approach of Smith and Dahlen (1973), the azimuthal anisotropic phase velocity $v_R(\omega, M, \Psi)$ of the dispersive surface waves with frequency ω at location M can be written as a Fourier series in azimuth Ψ as

$$\begin{aligned} v_R(\omega, M, \Psi) = \bar{v}_R(\omega) &+ a_0(\omega, M) \\ &+ a_1(\omega, M)\cos 2\Psi + a_2(\omega, M)\sin 2\Psi \\ &+ a_3(\omega, M)\cos 4\Psi + a_4(\omega, M)\sin 4\Psi, \end{aligned} \tag{2-13}$$

where $\bar{v}_R$ is an isotropic reference phase velocity, a_0 its isotropic lateral perturbation, $a_{1,2}$ and $a_{3,4}$ the coefficients for π-periodic and $\pi/2$-periodic azimuthal anisotropy, respectively. After Montagner and Nataf (1986), the $\pi/2$-periodicity is negligible small for Rayleigh type surface waves (i.e. for all vertical elliptically surface waves to generalize). Neglecting the higher periodicity and supposing a 1-dimensional depth model at the location of the reference model, the azimuthal perturbation of phase velocity $\delta v_R(\omega, M, \Psi) = \delta v_R(\omega, \Psi)$ can be approximated to

$$\delta v_R(\omega, \Psi) \approx a_C(\omega)\cos 2\Psi + a_S(\omega)\sin 2\Psi, \tag{2-14}$$

in which $a_{c/s}$ was introduced to denote the azimuthally anisotropic coefficients for cosine and sine term.
Montagner and Nataf (1986) show that Rayleigh-type surface wave velocity is most sensitive to elastic parameter L in case of short periods (this work deals with surface wave frequencies in a maximal range from 0.5 Hz to 10 Hz). Neglecting the contribution of the other parameters the surface wave phase velocity variation can thus be related to the anisotropic coefficients $G_C(z)$ and $G_S(z)$ via the sensitivity kernels $\partial v_R(\omega)/\partial L(z)$ as

$$\delta v_R(\omega, \Psi) \approx \int_0^Z \left[\frac{\partial v_R}{\partial L}(G_C\cos 2\Psi + G_S\sin 2\Psi)\right] \mathrm{d}z, \tag{2-15}$$

integrating from the surface to penetration depth Z. Comparing Eq. (2-14) and Eq. (2-15) and going from continuous depth towards a medium with layers $i = 1, ..., K$ we arrive at

$$a_{C/S}(\omega) \approx \sum_{i=1}^{K} \frac{\delta v_R(\omega)}{\delta L_i} G_{C/S_i}. \tag{2-16}$$

Assuming constant density within each layer, following Eq. (2-4) the perturbation in L can be expressed as $\delta L_i \approx 2\rho \bar{v}_{sv_i} \delta \bar{v}_{sv_i}$. For certain measured frequencies $\omega_j = \omega_1, ...\omega_N$, the reformulation in matrix-vector form yields

$$\begin{pmatrix} a_{C_1} \\ \vdots \\ a_{C_j} \\ \vdots \\ a_{C_N} \end{pmatrix} = \left[\frac{\delta v_R}{\delta L}\right]_{ji} \begin{pmatrix} G_{C_1} \\ \vdots \\ G_{C_i} \\ \vdots \\ G_{C_K} \end{pmatrix}, \quad \begin{pmatrix} a_{S_1} \\ \vdots \\ a_{S_j} \\ \vdots \\ a_{S_N} \end{pmatrix} = \left[\frac{\delta v_R}{\delta L}\right]_{ji} \begin{pmatrix} G_{S_1} \\ \vdots \\ G_{S_i} \\ \vdots \\ G_{S_K} \end{pmatrix}. \tag{2-17}$$

As for the body waves, the sensitivities can be calculated from the known isotropic velocity model and the anisotropic parameters can be inferred by inverting the system.

2-4 Merging the systems of surface and body waves

This work wants to improve the determination of subsurface anisotropic coefficients by adding information from surface waves to the evaluation of body wave splitting measurements. As both surface waves and body shear waves are governed by the same medium parameter, the two systems consist of equivalent model vectors and can elegantly be combined to carry out a joint inversion. To built a joint system, I suggest to merge Eq. (2-12) and Eq. (2-17) as follows:

$$\begin{pmatrix} a_{C_1} \\ \vdots \\ a_{C_N} \\ b_{C_1} \\ \vdots \\ b_{C_M} \end{pmatrix} = \begin{pmatrix} \left[\frac{\delta v_R}{\delta L}\right]_{ji} \\ \left[\sqrt{\frac{\rho}{L}}\frac{\delta z}{L}\right]_{ki} \end{pmatrix} \begin{pmatrix} G_{C_K} \\ \vdots \\ G_{C_i} \\ \vdots \\ G_{C_1} \end{pmatrix}, \quad \begin{pmatrix} a_{S1} \\ \vdots \\ a_{SN} \\ b_{S1} \\ \vdots \\ b_{SM} \end{pmatrix} = \begin{pmatrix} \left[\frac{\delta v_R}{\delta L}\right]_{ji} \\ -\left[\sqrt{\frac{\rho}{L}}\frac{\delta z}{L}\right]_{ki} \end{pmatrix} \begin{pmatrix} G_{S_1} \\ \vdots \\ G_{S_i} \\ \vdots \\ G_{S_K} \end{pmatrix}. \tag{2-18}$$

This joint system forms the main contribution of the present study. The inversion results will later be compared to the results of a sole body wave inversion. Beforehand, the next chapter shows how the parameters in the data vectors which describe azimuthally varying phase velocity and splitting intensity are extracted from the seismic data. Furthermore, the sensitivity kernels are addressed and the inversion algorithm is discussed.

Chapter 3

Data analysis and inversion: method

This chapter shows how the seismic data are analyzed in terms of splitting intensity SI and surface wave anisotropy. The analysis is carried out on the synthetic seismogram of a 1-dimensional depth model. Thereafter, the inversion algorithm is prepared, including a discussion on the sensitivity kernels of the surface and body waves.

3-1 Preparation of 1D-model and synthetic seismogram

To create synthetic data which can afterwards be analyzed and inverted, we want to set up an anisotropic 1-dimensional depth model. As a reference to build the 1D-model, I use the SEAM 'Barret Unconventional Model' (Oristaglio, 2014), which will also be used later in Chapter 5. For the parametrization of the 1D-model, the *Thomsen* parameters ϵ, γ, and δ are utilized (Thomsen, 1986). These 3 dimensionless parameters are very convenient to characterize a weak anisotropic material as ϵ is related to P-wave anisotropy, γ is related to the S-wave anisotropy, and δ is related to the anisotropy of the mixed terms. The full parametrization can be looked up in appendix A-1. Figure 3-1 and Figure 3-2 show the resulting depth functions.
After setting up the layered earth model, the synthetic seismic data is calculated in the program *ANIVEC* (Mallick and Frazer, 1990), which uses the Kennett invariant embedding procedure (Kennett, 2009). The modeling parameters correspond to a survey with receivers in a rectangular grid with maximal spread length of 3000 m and a central source.
The left hand side of Figure 3-3 contains the x-component of the PS-converted primaries from an explosive source with bandwidth from 0.5 Hz to 40.0 Hz and receiver time sampling of 4 ms. The 2 graphs on the right hand side show the radial and transverse component as functions of azimuth, extracted from a ring with offset range 240 m to 260 m (illustrated by the green lines on the left). The red boxes mark the reflection events SI1 to SI5 which will be evaluated in the body wave analysis in terms of SI. They correspond to the horizons at depth 1500 m, 2000 m, 2450 m, 2650 m, and 3100 m, respectively (see Figure 3-1 and 3-2). Note that the bright event at around 0.9 s (corresponding to the horizon at 950 m depth) is

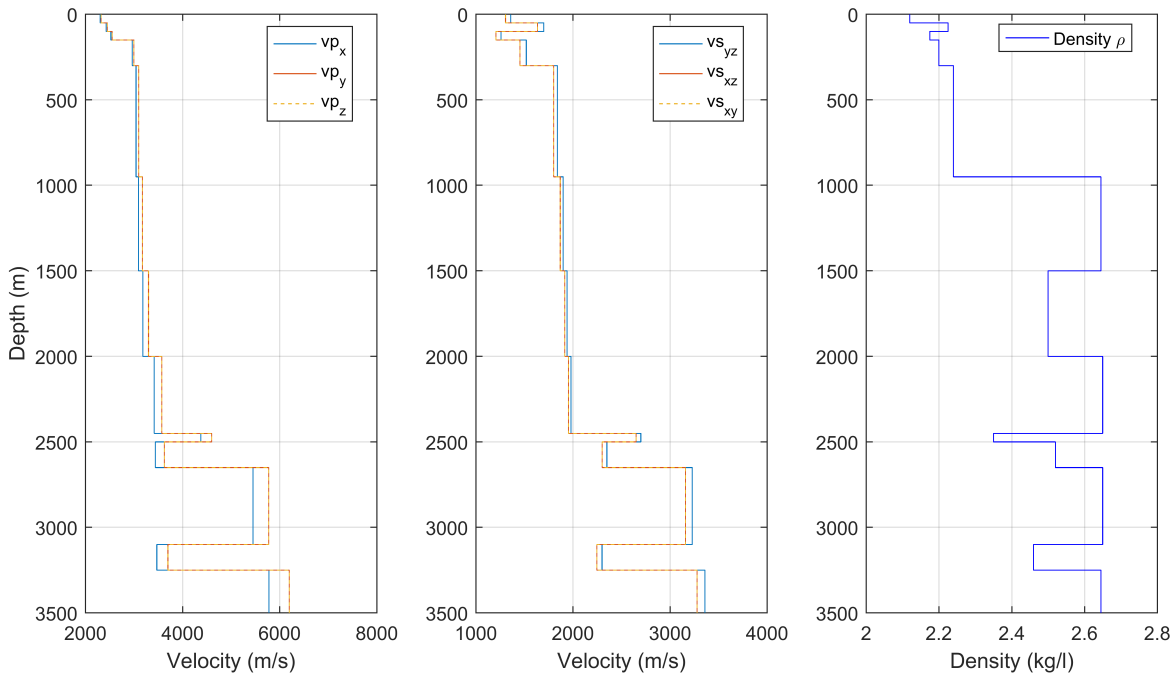

Figure 3-1: 1D-model depth parameter: P-wave velocities v_x, v_y, v_z (*left*), S-wave velocities v_{yz}, v_{xz}, v_{xy} (*middle*) and density ρ (*right*).

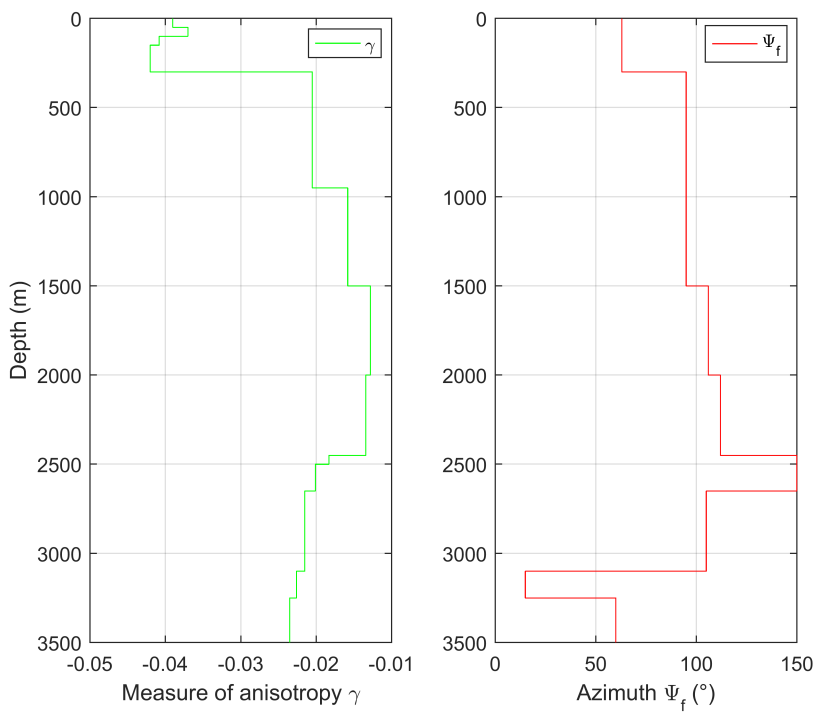

Figure 3-2: 1D-model depth parameter: *Thomsen* parameter γ (*left*) and fast axis direction Ψ_f (*right*).

contaminated by near-surface noise in the case of the 3D-model (see Figure 5-5). Due to this and due to the fact that the fast axis direction is not changing at the corresponding horizon (see Figure 3-2) the event will not be taken into account in the body wave analysis.

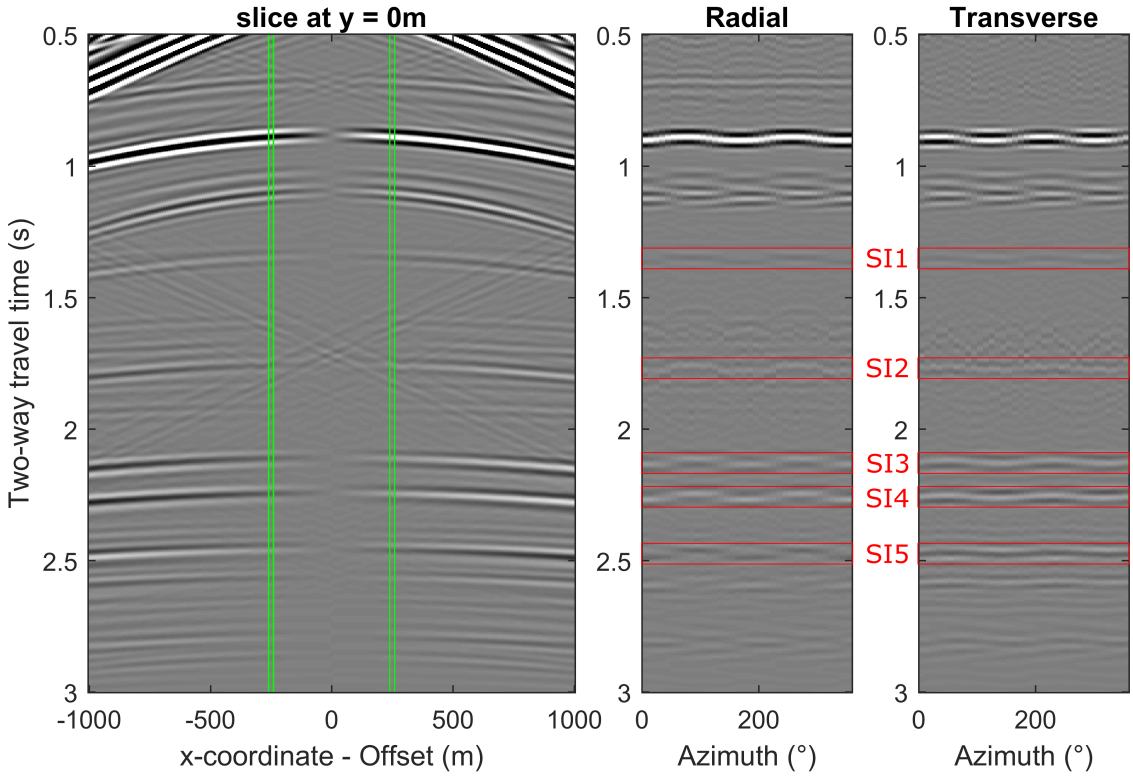

Figure 3-3: Synthetic seismogram of the 1D model (*left*): xz-plane slice of x-component PS-primaries response.Bandwidth ranges from 0.5 Hz to 40.0 Hz. *2 graphs on the right*: Radial and transverse component as functions of azimuth extracted form an offset range from 240 m to 260 m (illustrated by the green lines on the left graph). Red boxes mark the reflection events SI1 to SI5 for the SI-measurements.

Figure 3-4 shows the seismogram of the z-component for the full response from a vertical source with bandwidth from 0.5 Hz to 10.0 Hz and receiver time sampling of 4 ms. This response will be used for the surface wave analysis.

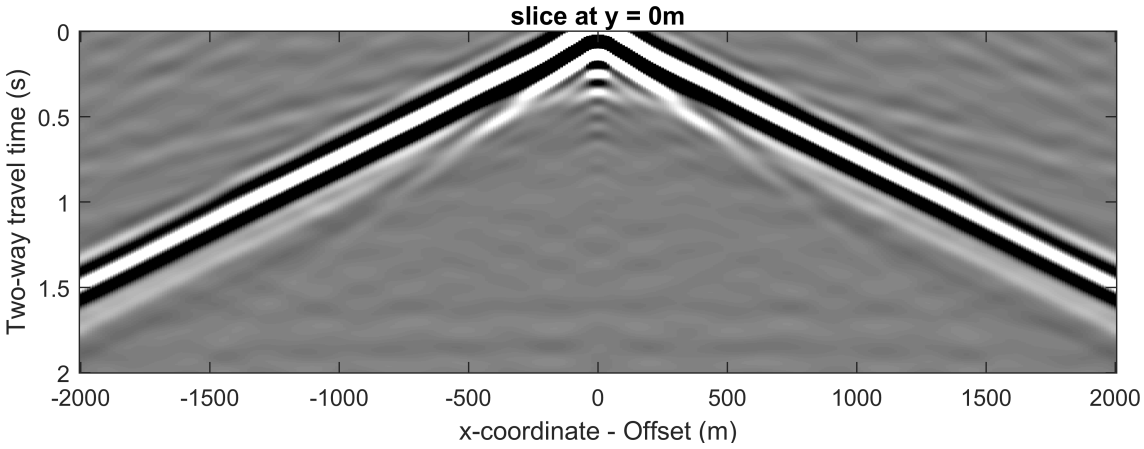

Figure 3-4: Synthetic seismogram of the 1D model: xz-plane slice of z-component full response. Bandwidth ranges from 0.5 Hz to 10.0 Hz. This data will be used for the surface wave analysis.

3-2 Splitting intensity measurement

To measure the shear-wave splitting, x- and y-component data in an offset range from 240 m to 260 m are extracted and transformed into radial and transverse component as already illustrated in Figure 3-3. The offset range is constraint in both direction: at too small offsets no PS-converted signals can be measured, at too large offsets the assumption of vertically traveling waves is violated. Figure 3-5 illustrates the data selection and shows radial and transverse component filtered with a low-pass up to 8 Hz.
Here, the characteristic patterns of shear-wave splitting are nicely visible. The radial component is varying in a sinusoidal way with azimuth: if the wave polarization is aligned with the fast axis, the arrival time is smallest, if it is aligned with the slow axis, the arrival time is largest. The transverse component shows a speckled pattern: if the polarization is aligned with either the fast or the slow axis, no splitting is taking place and no energy is on the transverse component.
Chevrot (2000) found a convenient way to measure the azimuthal variation in terms of splitting intensity SI. For delay times δt much smaller than the dominant wave signal periods, the radial and transverse component of the shear-wave (R and T, respectively) can be described as (Silver and Chan, 1991)

$$\begin{aligned} R(t) &\approx \omega(t), \\ T(t) &\approx -\frac{1}{2}(\delta\bar{t}\sin 2\bar{\beta})\,\dot{\omega}(t) =: -\frac{1}{2}SI\,\dot{\omega}(t), \end{aligned} \tag{3-1}$$

where $\omega(t)$ is the incoming wavelet and $\dot{\omega}(t)$ its time derivative. Eq. (3-1) reveals that for weak anisotropy the transverse component is equal to one half the negative time derivative of the radial component scaled by the term $\delta\bar{t}\sin 2\bar{\beta}$ which corresponds to the azimuthally varying total delay time in Eq. (2-9). This scaling term has been defined by Chevrot (2000) as the splitting intensity SI. Sieminski et al. (2008) show that the quantity SI is related to a time shift between radial component R and the sum of radial and transverse component $R + T$ which can be inferred by cross-correlation. Boiero and Bagaini (2016) extend this

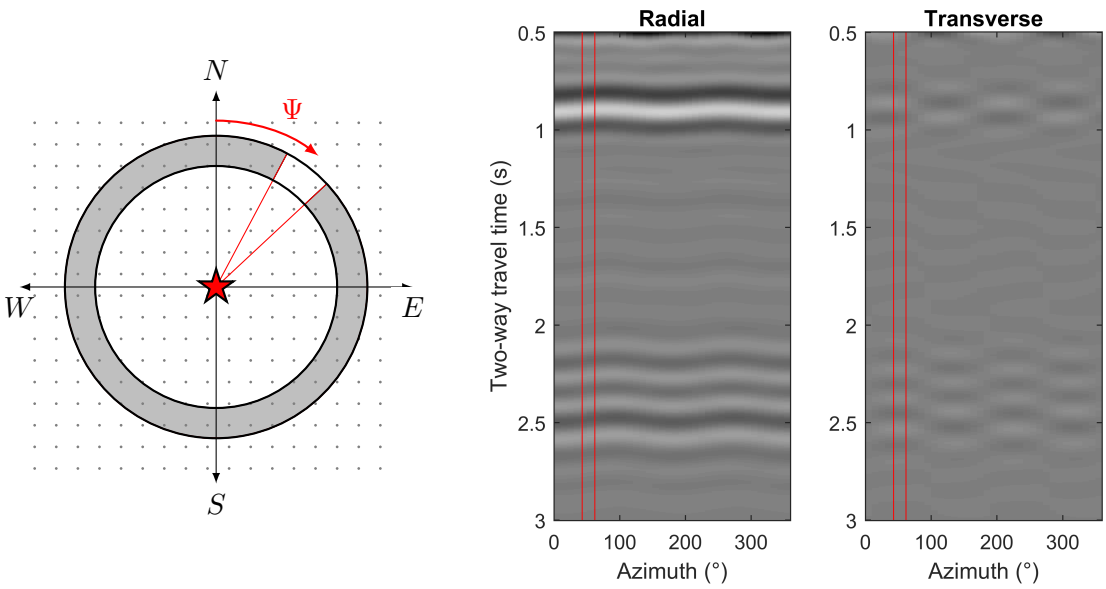

Figure 3-5: Extraction of data from a receiver grid (gray dots, 10 m spacing) within different azimuth sections: the gray ring illustrates the offset range of 240-260 m (*left*, the red star denotes the source). Radial component (*middle*) and transverse component (*right*) of the data after sorting by azimuth (the red lines correspond to the illuminated sector in the left graph).

concept and state that SI is equivalent to the lag between the sum $R+T$ and the difference $R-T$. This work will use the latter approach to determine the SI-values.
In order to not violate the assumption in Eq. (3-1) of small delay times compared to the signal periods, the low-pass filter up to 8 Hz is applied on the data as already displayed in Figure 3-5. With the just described method, the SI-values are determined in azimuth sectors of 10 ° for the events from SI1 to SI5. The azimuthally varying SI-values of each event are then fitted in a least-square procedure to a π-periodic sinusoidal curve in order to retrieve the Fourier parameters b_C and b_S as defined in Eq. (2-11). The corresponding measured SI-values for SI1 and SI5 and the their fits are displayed in Figure 3-6. It is obvious that the measured

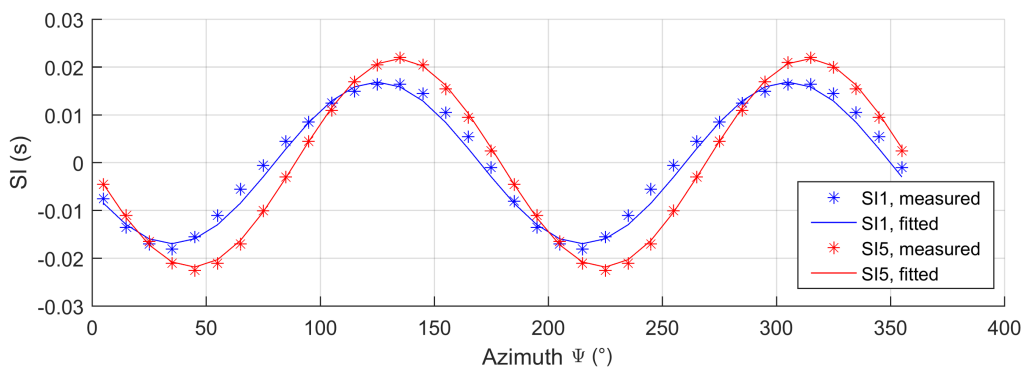

Figure 3-6: Splitting intensity SI-measurements for the reflection events SI1 and SI5. Asterisks denote the measurement picks, the solid lines are the π-periodic fits.

values exhibit a sinusoidal behavior and can hence be well fitted. Further, the zero-crossing from negative to positive values, which relates to the fast axis direction, is shifted between the events. This is in accordance with the model in Figure 3-2, where Ψ_f is slightly smaller in the layer above 1500 m compared to the layer above 3100 m.

3-3 Surface wave phase velocity measurement

For the surface wave analysis, the source-receiver geometry is sorted into sections of different azimuths. The signals of each azimuth section are stacked and transformed to the frequency-wavenumber (fk-) domain. This allows to analyze the wavenumber azimuthal distribution and from there calculate the phase velocity azimuthal variation. Figure 3-7 illustrates the data selection and shows the stacked data in the wavenumber domain at a certain frequency as a function of azimuth and in the fk-domain at a certain azimuth. Overlaid as a dashed purple line is the theoretical location of the first mode, derived directly from the model. We can conclude that the signals are in good accordance with the expected value and that no higher modes are present in the data.

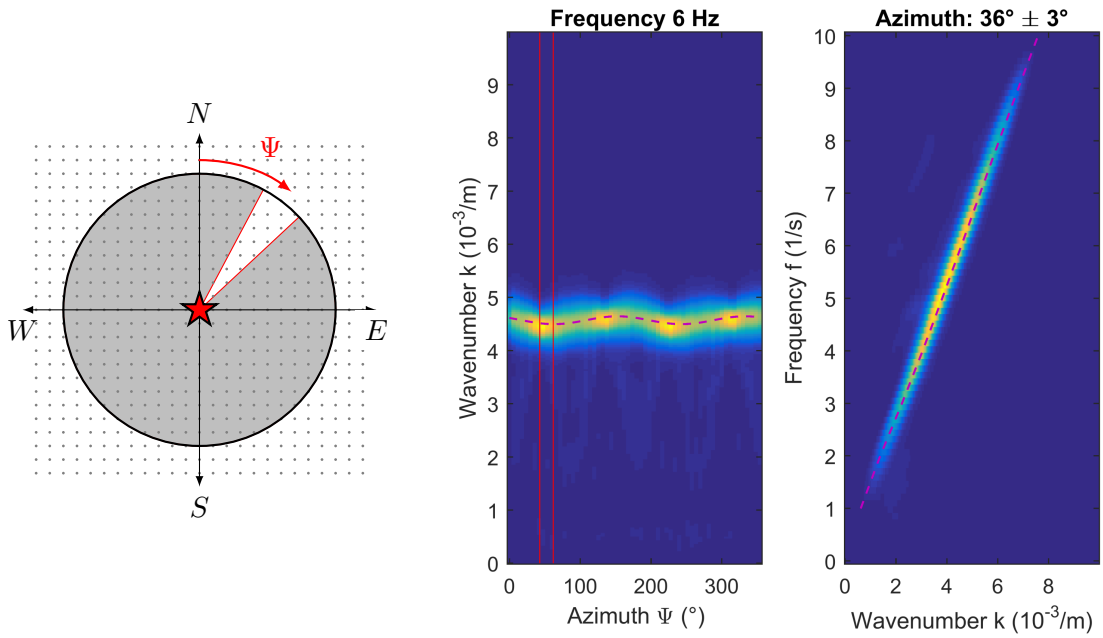

Figure 3-7: Illustration of the extraction process of the surface wave data (within the gray shaded disk of 2000 m radius) from a receiver grid (gray dots, 10 m spacing) in azimuths sections of 6° width (*left*, the red star denotes the source). Stacked data of frequency 6 Hz in the $k\Psi$-domain (*middle*, with the red lines corresponding to the illuminated sector in the left graph) and stacked data at azimuth $36° \pm 3°$ in the fk-domain (*right*). Overlaid the expected location of the 1st mode (dashed, purple).

For each frequency f, the wavenumber k is picked in the fk-domain. This is done by searching for the maximum within a specified wavenumber window. From this, the frequency- and

azimuth-dependent phase velocity is computed using the simple relationship

$$v_R(f, \Psi) = \frac{f}{k(\Psi)}. \tag{3-2}$$

This velocity corresponds to the surface wave velocity in 2-13. To determine the Fourier coefficients a_C and a_S and thereby the π-periodic azimuthal perturbation δv_R in Eq. (2-14), the calculated phase velocities are fitted in a least-square procedure to a π-periodic sinusoidal curve.

For the present the 1D-model, surface data is analyzed in a frequency range from 2.4 Hz to 9 Hz with intervals of 0.2 Hz. Figure 3-8 shows the measured values (asterisks) together with the fitted functions for frequency 4 Hz and 8 Hz.

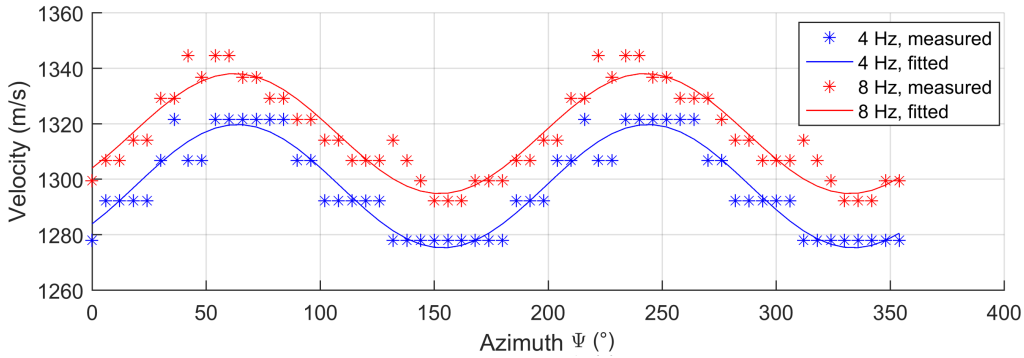

Figure 3-8: The azimuthal variation of the phase velocity v_R for frequencies 2 Hz and 8 Hz. Asterisks denote the measured values, calculated from the fk-pairs, the solid lines correspond to the π-periodic sinusoidal fits.

The azimuth of the maximum velocities align nicely with the fast axis direction of the prescribed model (see Figure 3-2). The fact that the lower frequency wave, which penetrates deeper, exhibits a lower velocity indicates the velocity inversion in the near-surface. Also visible is degraded velocity resolution for the lower frequency. This is related to the finite receiver spread, which limits the wavenumber resolution. Figure 3-9 shows, that lower frequencies correspond to smaller wavenumbers, which can be confirmed with Eq. (3-2) in case of similar velocity magnitudes (which can be assumed for the surface waves). Therefore, when looking at the velocity variation $\delta v_R = f/\delta k$, it becomes clear that the wavenumber variation δk is smaller at low frequencies. The limited wavenumber resolution results then in the poorer velocity resolution for lower frequencies.

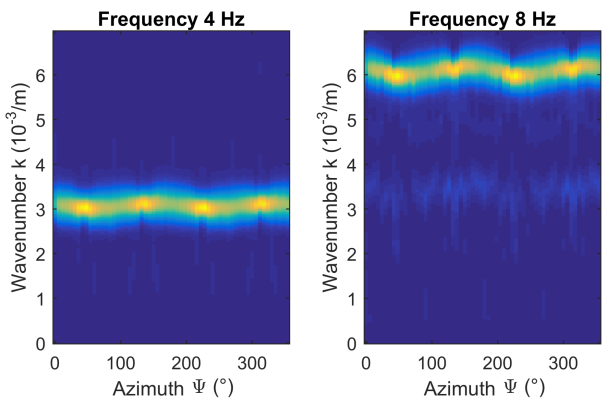

Figure 3-9: The wavenumber variation as a function of azimuth at surface wave frequencies 4 Hz (*left*) and 8 Hz (*right*). We can observe that the lower frequency signal is related to a smaller wavenumber and smaller wavenumber variation.

3-4 Sensitivities and inversion

3-4-1 Sensitivity kernels

The body wave sensitivities (see Eq. (2-12)) can straightforwardly be calculated from the isotropic velocity model and are shown on the right hand side of Figure 3-10 for all analyzed PS reflection events.
The sensitivity kernels for the surface waves (see Eq. (2-17))are calculated by perturbing the isotropic shear-wave velocity within a small range $\Delta\bar{v}_{sv}$:

$$\frac{\delta v_R}{\delta L} = \frac{1}{2\rho\bar{v}_{sv}}\frac{\delta v_R}{\delta\bar{v}_{sv}} = \frac{1}{2\rho\bar{v}_{sv}}\frac{v_{R+}(\bar{v}_{sv}+\Delta\bar{v}_{sv}) - v_{R-}(\bar{v}_{sv}-\Delta\bar{v}_{sv})}{2\Delta\bar{v}_{sv}} \tag{3-3}$$

Left hand side of Figure 3-10 shows the resulting sensitivity kernels of the surface waves in the frequency range from 2 Hz to 9 Hz.

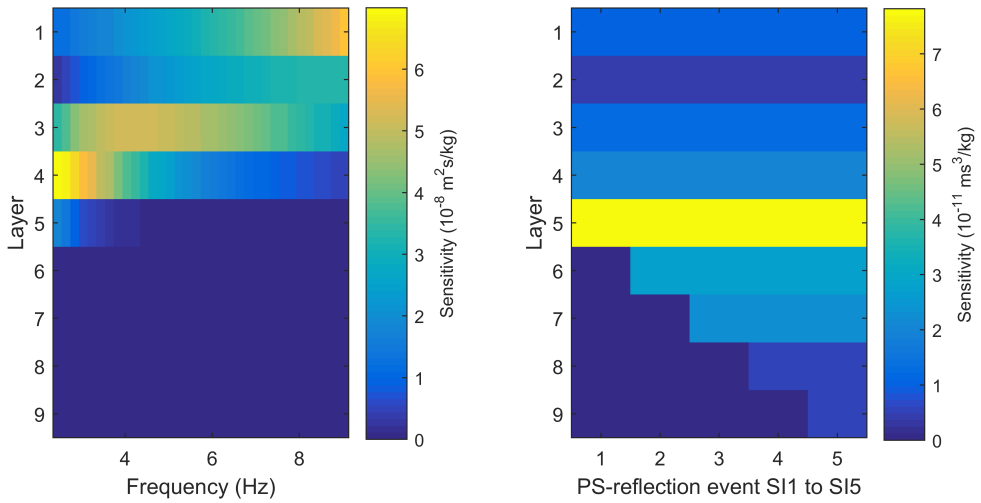

Figure 3-10: Layer sensitivities of surface waves dependent on their frequency (*left*) and of body waves for the different reflection events SI1 to SI5 (*right*).

3-4-2 Normalization of the sensitivity kernels

The magnitudes as well as the dimensions of the merged data from surface and body waves in Eq. (2-18) differ strongly (several meters per second compared to several milliseconds, respectively). Consequently, also the sensitivity kernels differ strongly in magnitude and dimension (see Figure 3-10), what causes difficulties for an overall regularization. In the following, two approaches of normalization are presented, seeking to balance out the differences.
In a first approach the system is normalized by the data input (Hering et al., 1995). While each entry of the data vector becomes one, each column of the Jacobian is divided by the data vector:

$$\mathbf{J'}_{ji} = \frac{\mathbf{J}_{ji}}{\mathbf{d}_j} \tag{3-4}$$

As a second approach, the system is normalized by the *RMS*-value of the columns of the Jacobian. To take care of the magnitude variations of surface and body wave data, a sub-Jacobian scaling is carried out as proposed by Manukyan et al. (2012)(here, the subsets relate to the different data parameters instead of the different model parameters):

$$\mathbf{J}'_{ji} = \frac{\mathbf{J}_{ji}}{\sum_{j \in \overline{Q}_d} \|\mathbf{J}_j\|}, \tag{3-5}$$

with $d = a_C, b_C$ and $\overline{Q}_d$ being a subset of Q which contains all data of type d.
Figure 3-11 compares the different normalization techniques on the sensitivity kernels of the 1D-model from above. For comparison, the sensitivity values are summed up across each layer. While the curve without normalization shows a significant kink after layer 5, where the surface wave sensitivity decreases towards zero, the normalization techniques equalize the sensitivity values across all layers. Here, data- and RMS-normalization give similar results in equalizing the magnitudes. In the following, the RMS-normalization is chosen as it gives the Jacobian a more convenient magnitude of order 10^0.

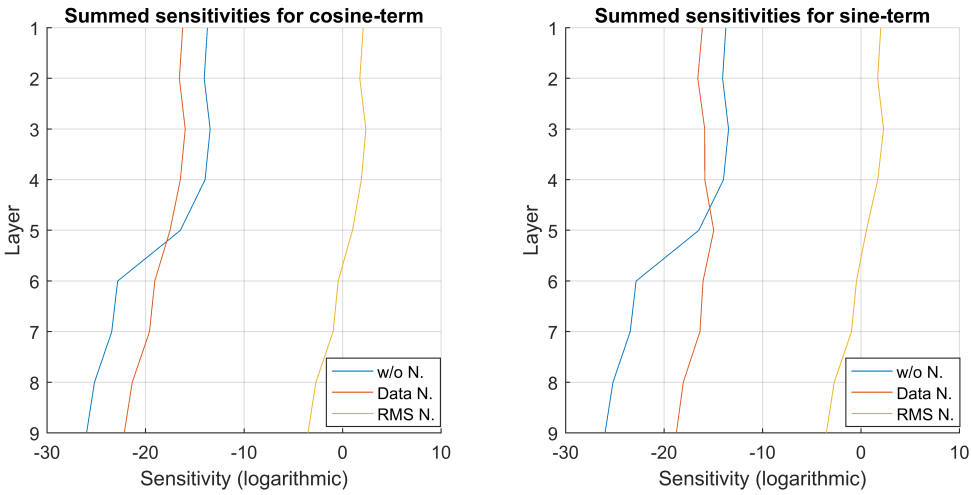

Figure 3-11: Sum of sensitivities over each layer for the cosine-system (*left*) and the sine-system (*right*) to compare the different normalization approaches: Data normalization (red) and RMS normalization (yellow). Note the logarithmic scale of the sensitivities.

3-4-3 Inversion algorithm

The sensitivity kernels are derived from the isotropic depth functions which are assumed to be known. Hence the Jacobian is independent from the anisotropic elastic coefficients. This allows, that the systems in Eq. (2-12), Eq. (2-17), and Eq. (2-18) can be solved directly without iterations. The normal equations for inverting the systems read

$$\mathbf{m} = (\mathbf{J}'\mathbf{W}'_\mathbf{e}\mathbf{W}_\mathbf{e}\mathbf{J} + \alpha_d^2\mathbf{W}_\mathbf{dw} + \alpha_s^2\mathbf{W}'_\mathbf{s}\mathbf{W}_\mathbf{s}\mathbf{W}_\mathbf{sw})^{-1}(\mathbf{J}'\mathbf{W}'_\mathbf{e}\mathbf{W}_\mathbf{e}\mathbf{d} + \alpha_d^2\mathbf{W}'_\mathbf{dw}\mathbf{m}^{\mathrm{ref}}), \tag{3-6}$$

where $\mathbf{m}$ and $\mathbf{d}$ are model- and data-vector, respectively, $\mathbf{J}$ is the sensitivity kernel, $\mathbf{W_e}$ contains the data errors, α_d and α_s is damping and smoothing parameter, respectively, and $\mathbf{W_s}$ is the smoothing matrix. $\mathbf{W_{dw}}$ and $\mathbf{W_{sw}}$ are weighting matrices for the regularization and will be utilized to apply damping constraints inversely proportional to depth or smoothing constraints inversely proportional to layer thickness. $\mathbf{m}^{\text{ref}}$ is the reference model towards which the solution can be damped. Here, the reference model corresponds to the isotropic model without anisotropic perturbations which means $\mathbf{m}^{\text{ref}} = 0$.
To find the solution an appropriate fit between observed data $\mathbf{d}^{\text{obs}}$ and predicted data $\mathbf{d}^{\text{pred}}$ within the estimated data error ε,the objective function Φ_d is optimized to equal 1:

$$\Phi_d = \frac{1}{N} \sum_{i=1}^{N} \left(\frac{d_i^{\text{obs}} - d_i^{\text{pred}}}{\varepsilon_i} \right)^2 . \tag{3-7}$$

The next Chapter presents and compares the inversion results for the 1D-model. Subsequently, the results are used to correct the seismic data for the effect of SWS.

Chapter 4

1D-model: inversion results and shear-wave splitting compensation

This chapter shows the inversion results for the 1D-model. After evaluating the body wave data and the surface wave data separately, they are combined in the joint inversion. From the deduced elastic coefficients, the azimuthal velocity is calculated.

4-1 Body wave inversion

After estimating the SI values for several reflected events, describing their azimuthal variation with Fourier coefficients and calculating the Jacobian from the isotropic velocity model, the inversion can now be performed. Thus, with normal Eq. (3-6) by hand, the system in (2-12) is solved. The data error is chosen to be 1% of the data values. It is increased to 2% for the uppermost event, as the uncertainty is expected higher due to the near-surface noise and less data coverage. As no SI data is present for the shallow layers, regularization is introduced in order to prevent the model parameters to go out of control for those layers. The two graphs on the left hand side of Figure 4-1 show the data points with error bars together with the predicted data from the inversion. The inversion is able to fit the data very well. The two graphs on the right hand side show the inversion results in terms of the anisotropic elastic coefficients G_C and G_S and display them together with the true model parameters. Compared to the shallow layers down to layer 4, a generally better agreement can be observed from layer 5 on, where SI measurements are available. In the deepest part, namely layer 8 and 9, the inversion is not well fitting the true parameters.
From the anisotropic coefficients G_C and G_S, the azimuthal anisotropic shear-wave velocity v_{sv} is determined following Eq. (2-7), as well as the the fast axis direction Ψ_f and the relative velocity variation $\delta v_{sv}/\bar{v}_{sv}$ (Eq. (2-8)). Figure 4-2 displays these variables.
The already discussed inversion results can here be observed once again: the shallow 4 layers down to 300 m do not well agree with the true model. The result for layer 5 agrees well in terms of fast axis direction, whereas the magnitude of anisotropy is overestimated. This is

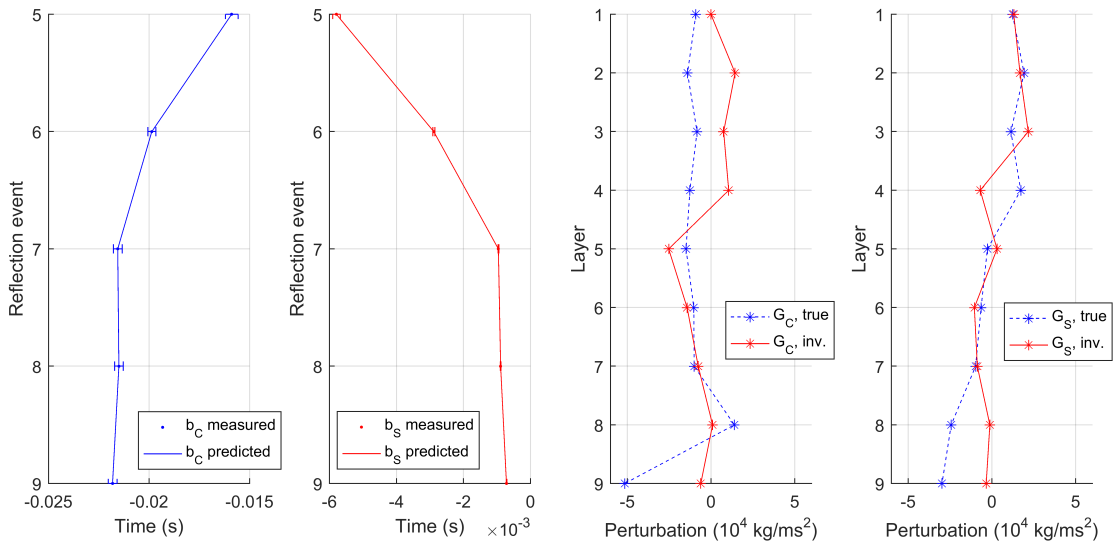

Figure 4-1: *2 graphs on the left:* Comparison between measured and predicted data coefficients b_C and b_S. The measured data contain error bars. *2 graphs on the right:* Comparison between inversion results and true model parameter for the anisotropic coefficients G_C and G_S.

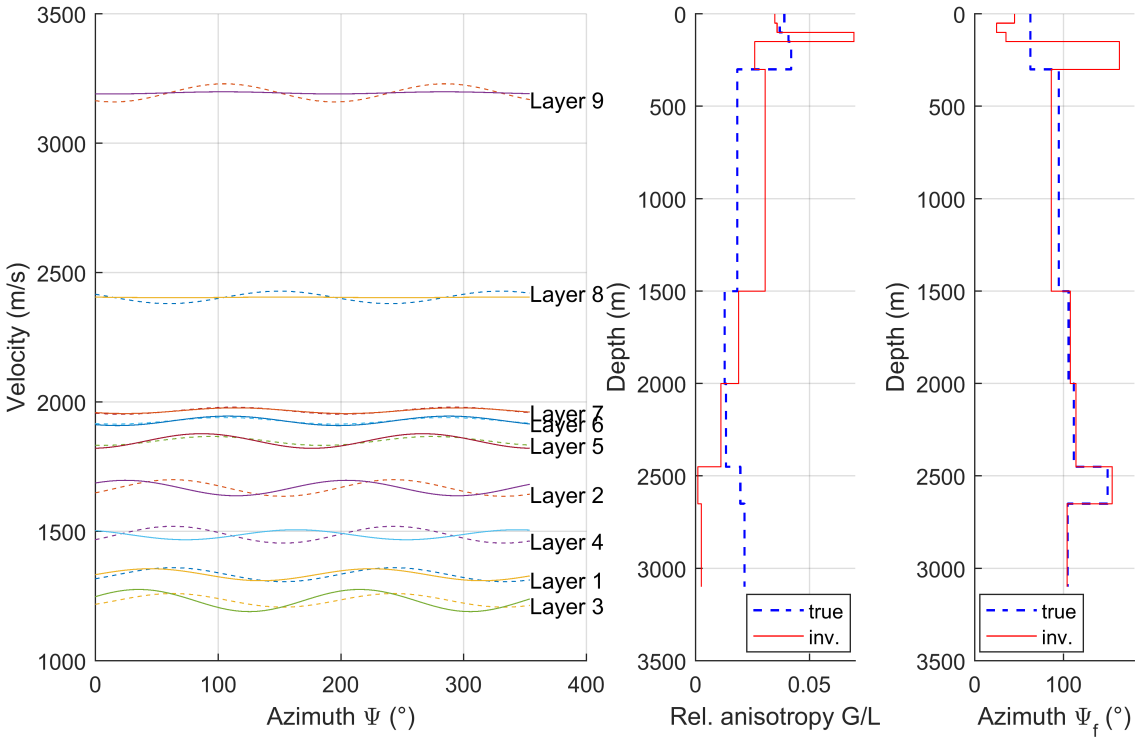

Figure 4-2: *Left*: Layered anisotropic velocity from inversion (solid lines) compared with the true model velocity (dashed lines). Relative shear-wave anisotropy G/L (*middle*) and fast axis direction Ψ_f (*right*) from true model and inversion results.

caused by the influence of the shallow layers, which bias the SI measurement. The deeper part are reasonably well resolved except for the anisotropy amplitude in the two deepest layers. The incomplete amplitude recovery might be explained with the low frequency signals, which are not able to resolve thin layers. This is can be observed in the seismograms in Figure 3-5, in which the reflection events in the deeper part are overlapping due to the low frequency.
It is expected that the observed misfit in the shallow part down to layer 5 can be corrected by including the data from the surface waves. Before performing the joint inversion, an inversion of the surface waves only will be carried out and evaluated.

4-2 Surface wave inversion

The procedure for the surface wave inversion is analogue to the body wave inversion. The system (2-17) for the surface waves is solved with the normal equation in (3-6). Data input are the Fourier coefficients a_C and a_S which describe the azimuthal varying phase velocities. The data error is estimated to decrease linearly from 1 m/s for the lowest frequency (2.4 Hz) to 0.5 m/s for the highest frequency (9 Hz). The left hand side of Figure 4-3 shows the data input with error bars as well as the predicted data from the inversion. The data is fitted reasonably well within the corresponding uncertainties. The two graphs on the right hand side compares the inverted anisotropic elastic coefficients G_C and G_S true model parameters. Especially the inverted G_S is in good agreement with its true counterpart. G_C is slightly off for the inner layers. This might be related to the strongly varying sensitivities (see Figure 3-10) due to the changing velocities and densities of the layered model (see Figure 3-1).

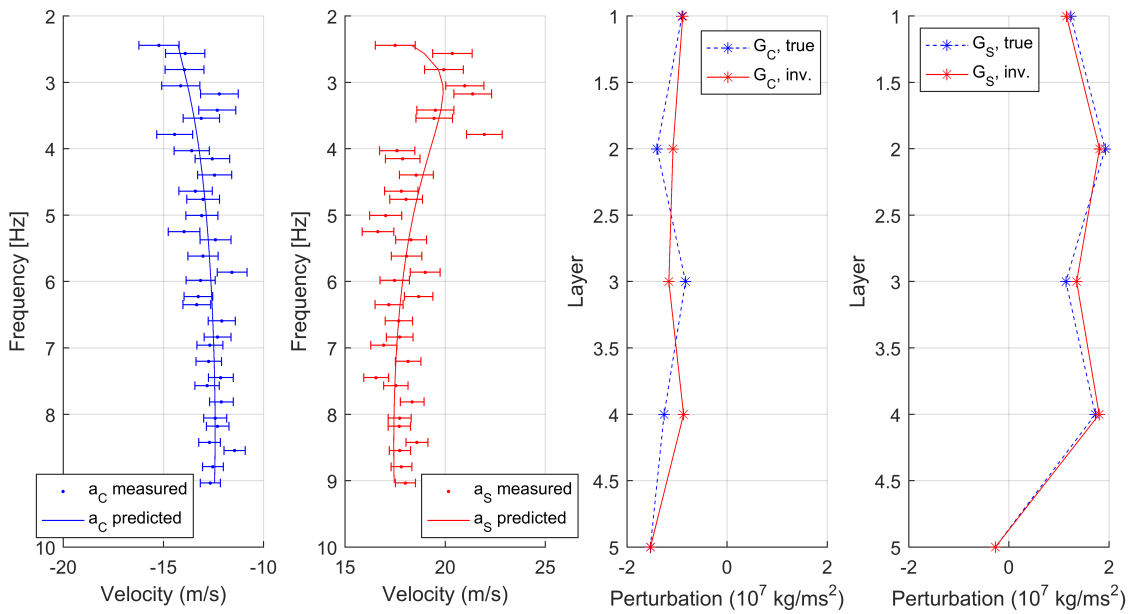

Figure 4-3: *2 graphs on the left:* Comparison between measured and predicted data coefficients a_C and a_S. The measured data contain error bars. *2 graphs on the right:* Comparison between inversion results and true model parameter for the anisotropic coefficients G_C and G_S.

Nevertheless, the inferred azimuthally varying velocities, displayed in Figure 4-4, show good agreement with the true model. The two graphs on the right hand side confirm the agreement to the true model. The only exception is the deviation of the anisotropy magnitude in the third layer.

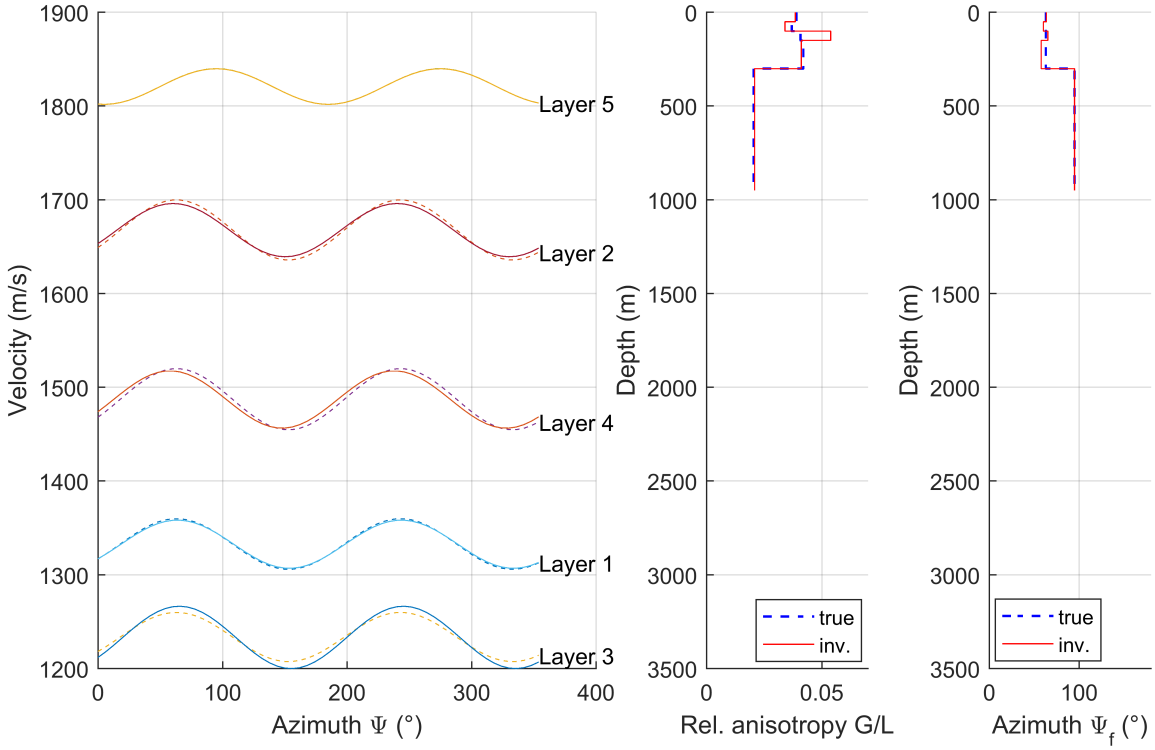

Figure 4-4: *Left*: Layered anisotropic velocity from inversion (solid lines) compared with the true model velocity (dashed lines). Relative shear-wave anisotropy G/L (*middle*) and fast axis direction Ψ_f (*right*) from true model and inversion results.

4-3 Joint inversion

Body wave SI measurements and surface wave phase velocity variations are finally jointly inverted for the anisotropic elastic coefficients G_S and G_C. Analogue to the inversion procedures before we take the normal equation in (3-6) to solve the joint system (2-18).
Figure 4-5 displays the data with error bars and the corresponding predicted data from the inversion. The joint inversion is fitting the data as well as the separate inversion procedures before. The two graphs on the right hand side of Figure 4-5 show the inverted and the true model parameters G_S and G_C. Compared with the results of the sole body wave inversion in Figure 4-1 a significant improvement is observable: the shallow part reveals a much better agreement with the true model.
The improvement becomes also evident looking at the inferred velocity variations, the measure of anisotropy G/L and the fast axis direction Ψ_f, illustrated in Figure 4-6. Through the inclusion of the surface waves, the strong deviations in the shallow part in the body wave

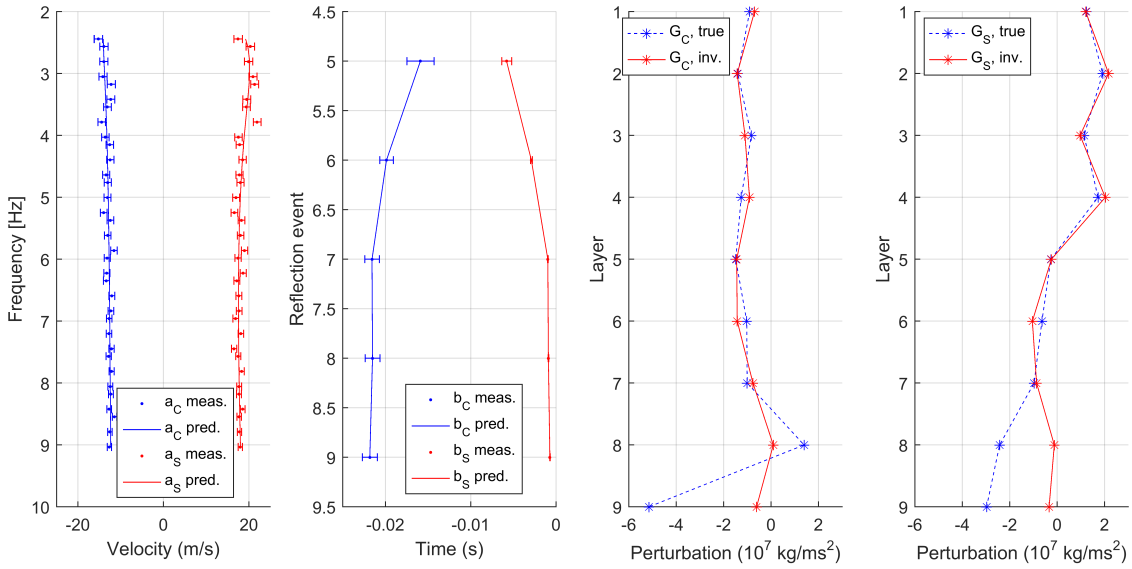

Figure 4-5: *2 graphs on the left:* Comparison between measured and predicted data coefficients a_C, a_S and b_C, b_S. The measured data contain error bars. *2 graphs on the right:* Comparison between inversion results and true model parameter for the anisotropic coefficients G_C and G_S.

inversion are now minimized. Deviations from the true model can still be recognized for the deeper layers. However, we did not expect them to be eliminated in the joint inversion.
To conclude the section of the joint inversion on the 1D-model, we can state that the inclusion of the surface waves improved the results for the shallow part as expected. We shall now demonstrate the improvement by compensating the seismogram for SWS applying the inversion results and thus enhancing the image quality.

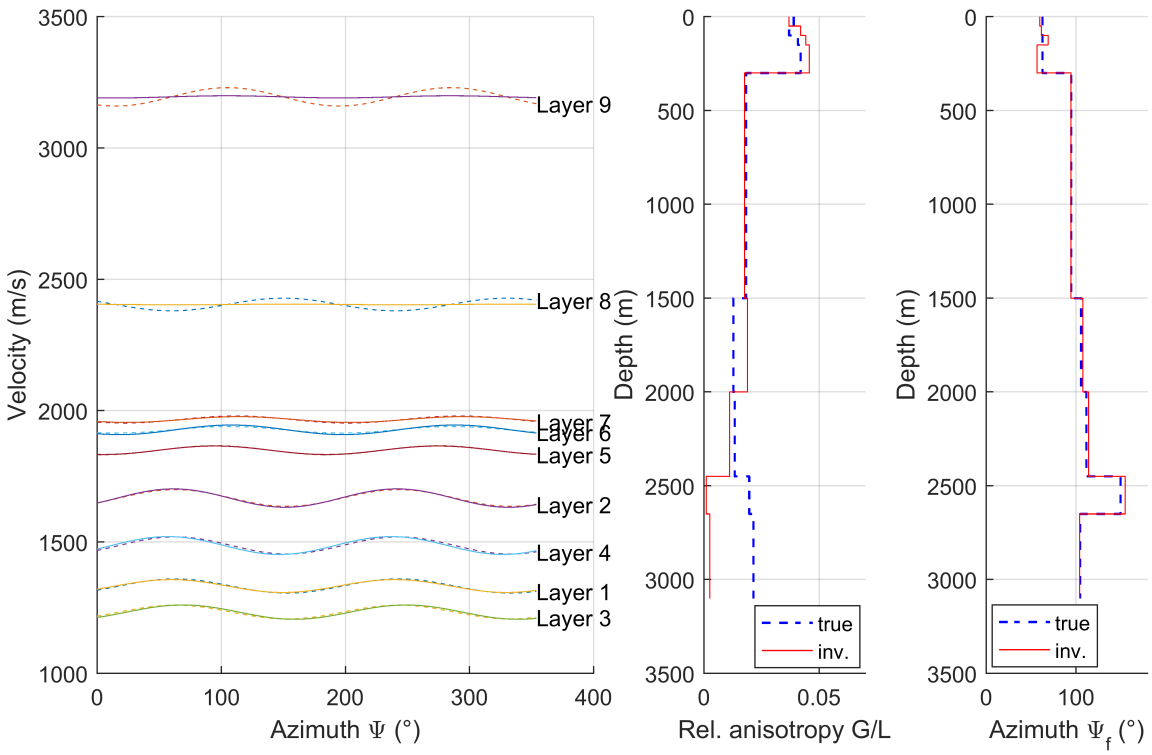

Figure 4-6: *Left*: Layered anisotropic velocity from inversion (solid lines) compared with the true model velocity (dashed lines). Relative shear-wave anisotropy G/L (*middle*) and fast axis direction Ψ_f (*right*) from true model and inversion results.

4-4 Shear-wave splitting compensation

This section makes use of the inversion results above and aims to correct for the effect of SWS. More precisely, the delay time δt between fast and slow axis and the fast axis direction Ψ_f is calculated with the help of the inverted anisotropic coefficients. Subsequently, the splitting effect is compensated layer by layer in a so-called layer-stripping procedure. The correction is carried out on a PS-signal section similar to the one shown in Figure 3-5 with radial and transverse component as a function of the azimuth and frequency content up to 40 Hz. We expect through the SWS compensation, that the sinusoidal reflection events on the radial component will become flat and that the energy on the transverse component will become zero.
Primarily, the results from the sole body-wave inversion are used for the compensation. Figure 4-7 compares the uncorrected section with the PS-inversion corrected section. Note that all graphs are displayed in the same scale.

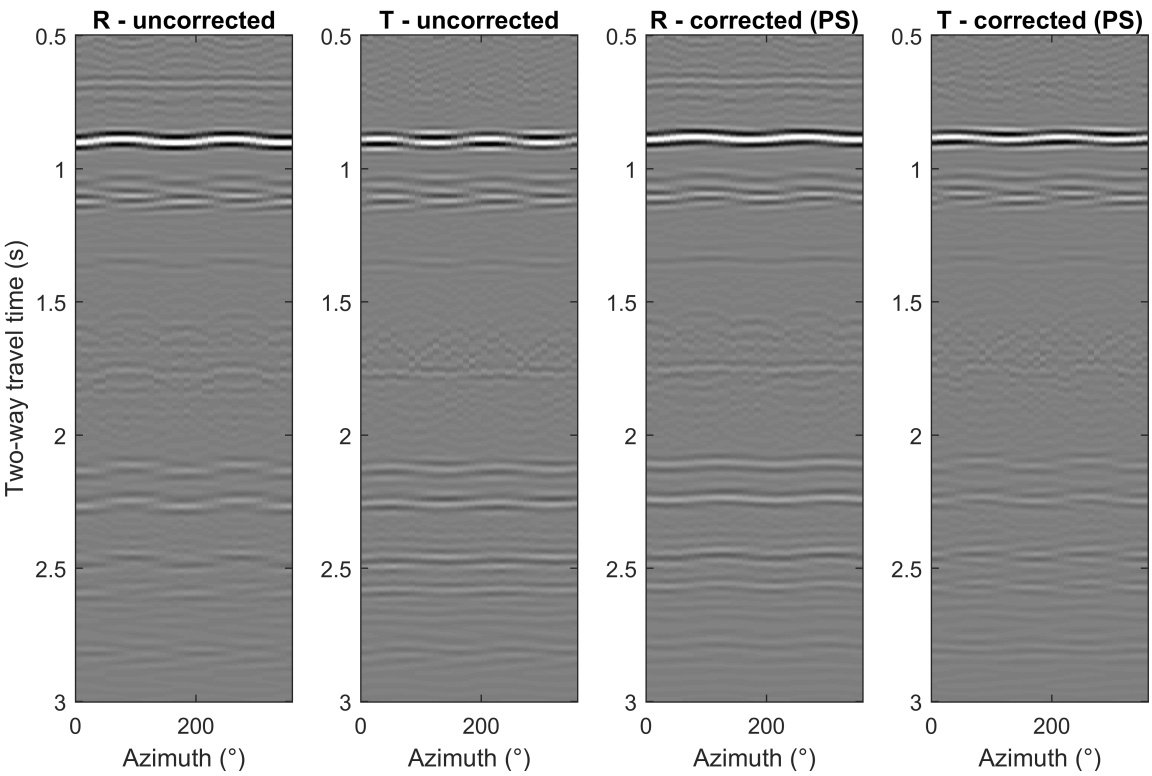

Figure 4-7: Azimuthally varying PS-signals on radial (R) and transverse (T) component: uncorrected (*2 graphs on the l.h.s.*) and corrected using the results of the body-wave inversion (PS, *2 graphs on the r.h.s.*).

Even though the sinusoidal character of the events remains and considerable energy is left on the transverse component, improvements are evident. Take for example the event at two-way travel time (TWT) around 1.75 s: while it is hardly visible within this rather noisy region on the radial component, it clearly appears after the SWS compensation. Vice versa on the transverse component: energy which can be seen on the uncorrected section disappears after compensation. However, as the first SI measurement (SI1) is from the event at around 1.35 s,

information on the anisotropy for earlier events is missing. These events cannot be corrected and influence the deep events due to the cumulative nature of the delay time.
Next, we use the results from the joint inversion to correct for SWS. Figure 4-8 displays both the compensation with the results form the body-wave inversion and the compensation with the results from the joint inversion. The improvements from the joint inversion are tremendous. Through the inclusion of the surface wave data, the early event at about 0.9 s is flattened on the radial component and its energy is strongly reduced on the transverse component. The later arrivals benefit similarly from the compensation in the shallow part. It is also quite interesting to study the event at around 1.1 s which in an internal multiple (observe the different move out in the seismogram on the left hand side of Figure 3-3). Due to the double transition through the anisotropic layer, the delay time between fast and slow traveling signal increases. The SWS-correction does not compensate for this, which is why a sinusoidal behavior on the radial component and significant energy in the transverse component remain.

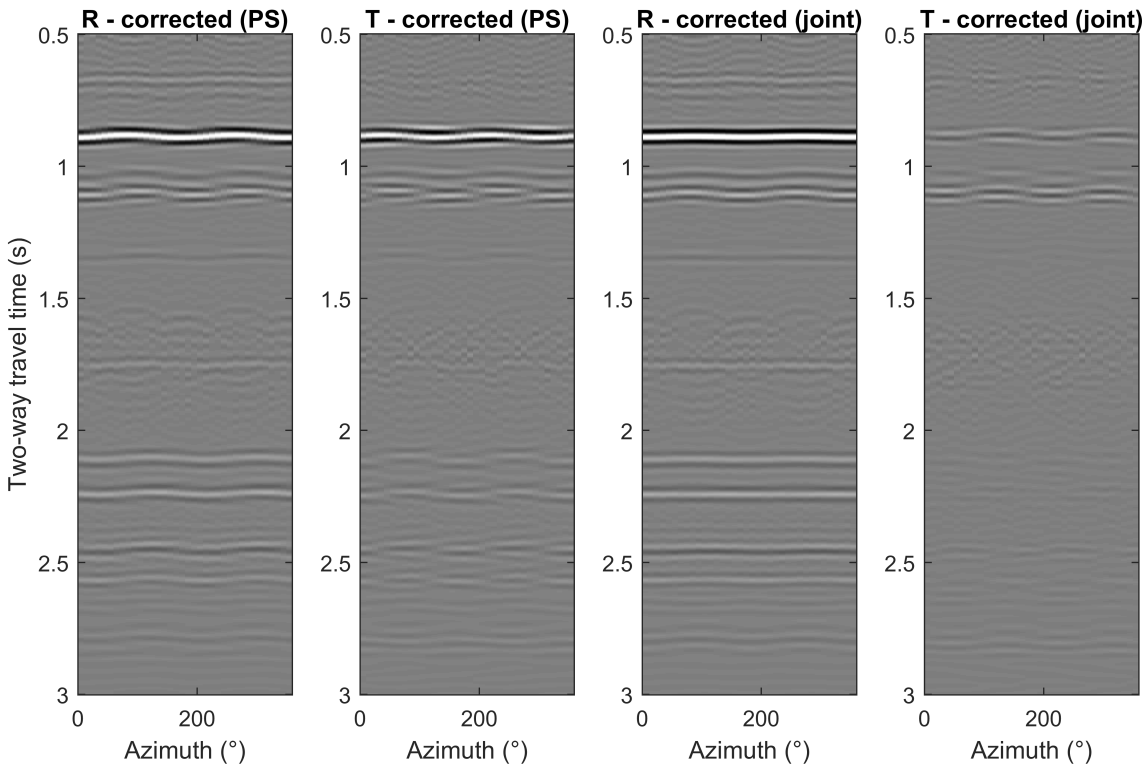

Figure 4-8: Azimuthally varying PS-signals on radial (R) and transverse (T) component: corrected using the results of the body-wave inversion (PS, *2 graphs on the l.h.s.*) and corrected using the results of the joint inversion (joint, *2 graphs on the r.h.s.*).

Finally, we want to compare the compensation using the results of the joint inversion with the exact compensation using the theoretical delay times and the true fast axis directions from the model. This comparison is shown in Figure 4-9. While it is very hard to spot any differences on the radial component, the transverse component helps to detect some discrepancies. So for example the energy remaining of the event at about 0.9 s. Less energy is left in case of the correction with the true parameters. The fact that still some energy is visible

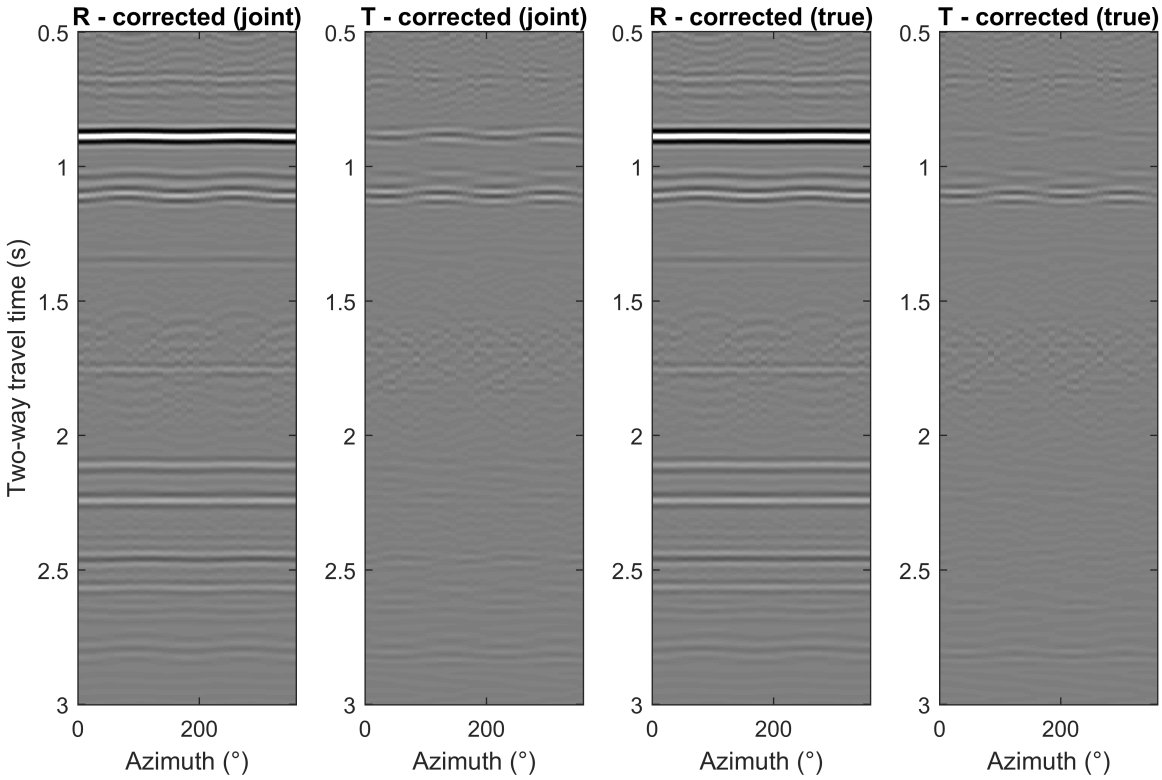

Figure 4-9: Azimuthally varying PS-signals on radial (R) and transverse (T) component: corrected using the results of the joint inversion (joint, *2 graphs on the l.h.s.*) and corrected using the theoretical SWS-values (true, *2 graphs on the r.h.s.*).

might be related to an imperfect reconstruction of the near-surface parameters which can result from the nature of surface waves penetrating across several layers and hence build a mixed-determined problem. Further on, for the later arrivals, the joint inversion results lead to a basically spotless compensation. Merely in the part after about 2.4 s, the compensation becomes slightly weaker. This is most likely to the not fully recovered anisotropy magnitude for those events.

Generally we can conclude, that the SWS-compensation is notably improved using the results from the joint inversion as compared to the results form the body-wave inversion. The incorporation of the surface waves adds important information for the near-surface, which is needed not only to correct the early events but also to correct the entire time section.

Chapter 5

3D-model: set-up and inversion

This chapter expands the study on anisotropic shear-wave velocity towards a more realistic setting. For this, an anisotropic 3-dimensional Earth model is created based on the SEAM 'Barrett Unconventional Model'. Then, after calculating synthetic seismograms for the model, the joint inversion shall be tested and compared to the inversion of only PS data.

5-1 Set-up of the 3D-model

The 'Barrett Unconventional Model' of the SEG Advanced Modeling (SEAM) Corporation was primarily created to model seismic anisotropy of fractured shale reservoirs and is hence a perfect starting point for a realistic anisotropic 3D-model for the present study. The Barrett Model imitates the geologic region of the Arkoma Basin in the Midwestern United States (Oristaglio, 2014). It consists of a near surface zone in the upper 300 m, followed by an stratigraphic sequence of quasi-parallel sand, shale, and shaley-sand layers with penetrating meandering stream channels. This overburden reaches a depth of about 2.5 km, at which the reservoir region with two organic-rich shale layers begins. The whole sequence below the near surface zone is traversed by two major faults.
All the discussed features can be observed in Figure 5-1, which displays the S-wave velocity distribution along two depth slices. The red lines identify horizons H1 to H7 which constrain the layers needed to set up the model and the inversion. H1 to H4 have constant depth of 100 m, 200 m, 300 m and 400 m, respectively. Figure 5-2 displays the density distribution on the same depth slices.
The Barrett Model introduces rock anisotropy at reservoir region, where densely spaced fine vertical fracture cause an HTI symmetry. For the purpose of the present study we want anisotropy throughout the model including the near surface zone, which shall be resolved with the help of the surface waves. Therefore, I defined the Thomsen parameter γ (which controls the S-wave velocity anisotropy) on the whole section down to reservoir depth according to the stratigraphic structure. The distribution of γ is displayed in Figure 5-3 on the same depth slices as before. It can be observed that the near surface is now strongly anisotropic.

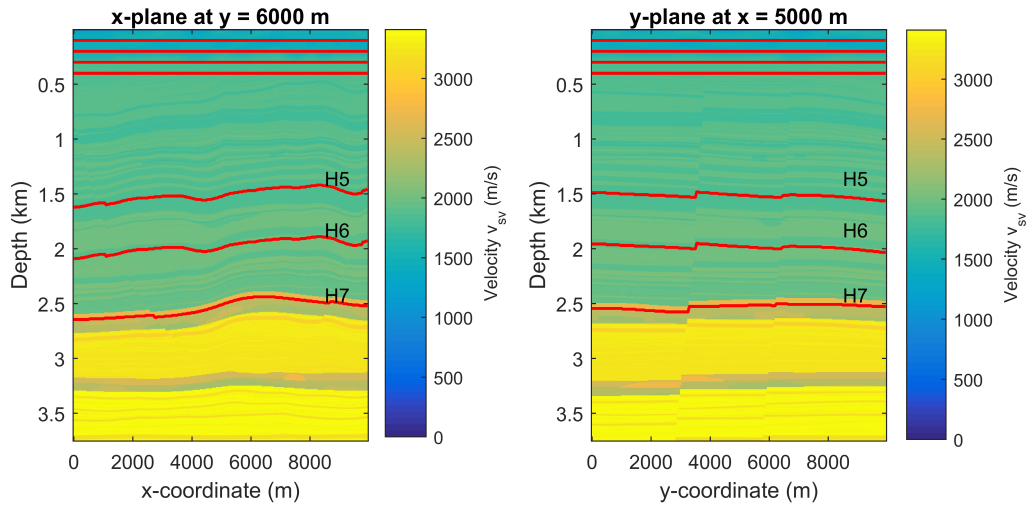

Figure 5-1: S-wave velocity v_{sv} distribution within two orthogonal depth slices in the x-plane (*left*) and the y-plane (*right*). The red lines define the shallow horizons H1 to H4 with constant depth from 100 m to 400 m and the deeper horizons H5 to H7. Note that H7 corresponds to the top of the reservoir.

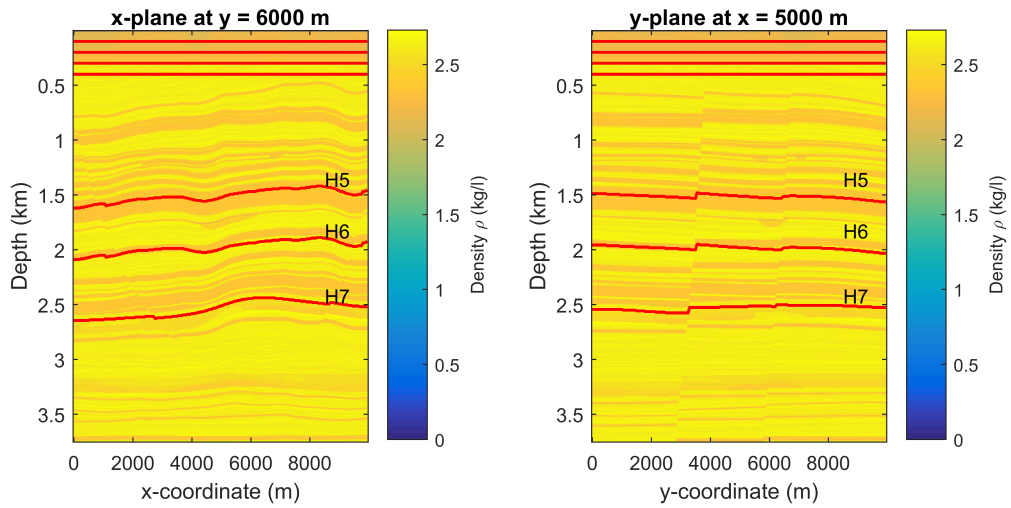

Figure 5-2: Density ρ distribution within two orthogonal depth slices (similar as in Figure 5-1). The red lines mark horizons H1 to H7.

To fully characterize the rock anisotropy, its orientation is still left to be defined. I decided to define four blocks of different HTI orientation, namely the first block down to horizon H3 at 300 m depth (i.e. the near-surface zone), followed by 3 blocks down to horizons H5, H6, and H7, respectively. Within these blocks, the orientation of the anisotropy is defined according roughly to the velocity structure. This is shown in Figure 5-4, in which the fast axis direction Ψ_f is marked with the red line and plotted over the overall velocity of the displayed zone. Several features can be observed. The anisotropy of the shallowest block (here displayed over the overall velocity between H2 and H3) exhibits a circular behavior. Such a behavior can for instance be caused by subsidence above a produced reservoir. For the deeper blocks, the fast

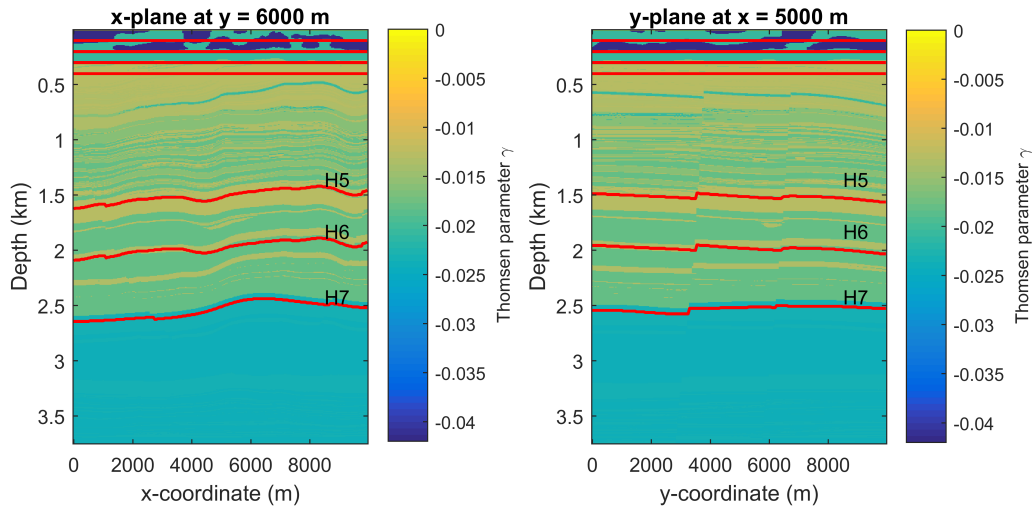

Figure 5-3: Magnitude of anisotropy, denoted by Thomsen parameter γ, within two orthogonal depth slices (similar as in Figure 5-1). The red lines mark horizons H1 to H7.

axis is roughly aligned in East-West direction. Besides, the 2 major faults can be recognized in the velocity distribution as well as the mentioned meandering channels.

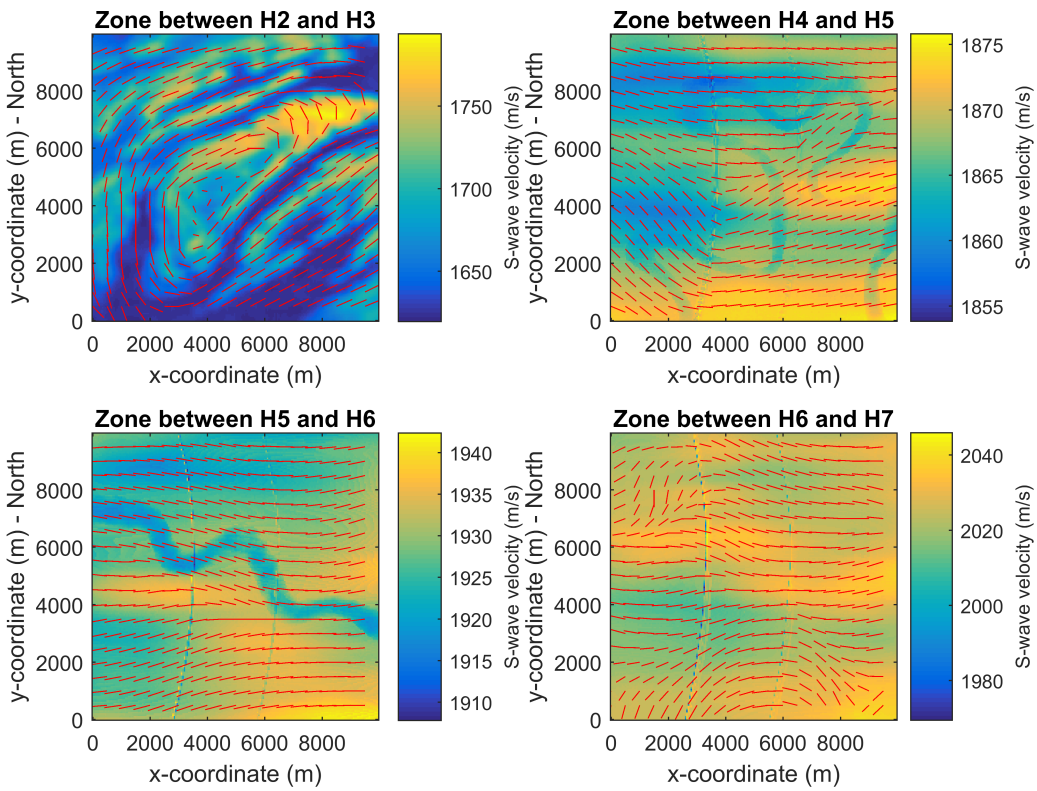

Figure 5-4: Fast axis direction Ψ_f (red lines) in the defined blocks down H4 (top left), H5 (top right), H6 (bottom left), and H7 (bottom right). The background shows the average S-wave velocity of the corresponding zone.

5-2 Synthetic seismogram and data acquisition

The seismic data for the 3D-model is created using a finite difference modeling code (Lisitsa and Vishnevskiy, 2010). Figure 5-5 displays a section of the corresponding seismogram.

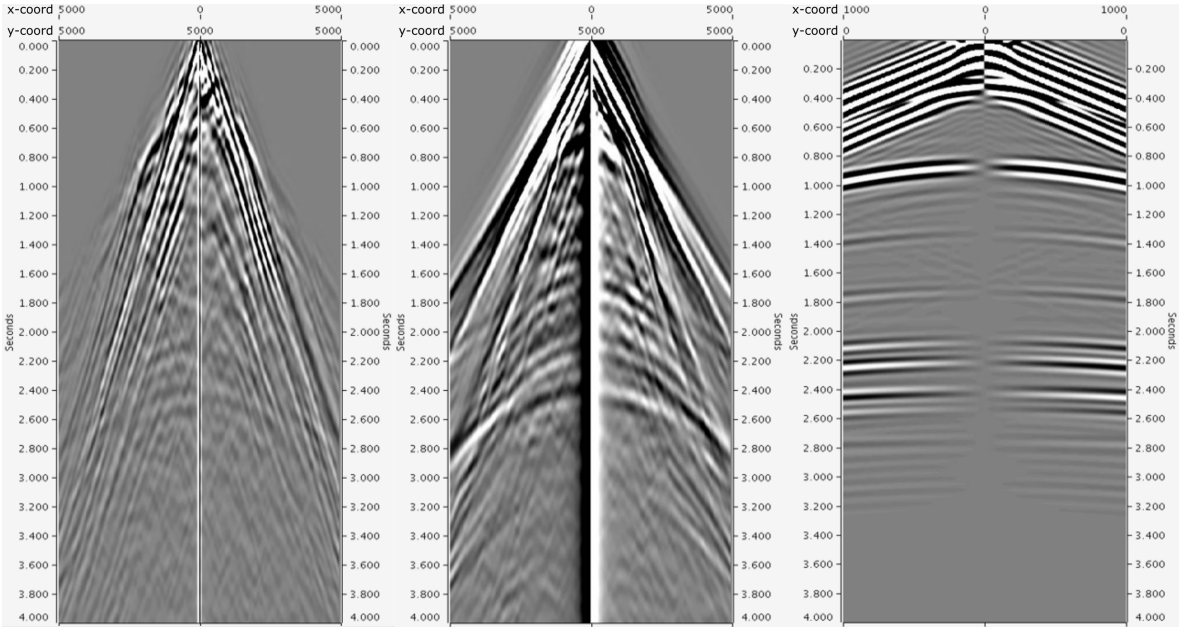

Figure 5-5: x-component (*left*) and y-component (*center*) of the modeled data from the 3D-model (seimograms show y-slices at $x = 0\,\mathrm{m}$). *Right:* The corresponding section of the modeled data from the 1D-model.

Subsequently, a regular grid of 19x19 positions (spread in a range from 500 m to 9500 m in both x- and y-coordinate with 500 m spacing) is defined on the surface area. At each position the surface wave phase velocity and the splitting intensity SI is measured as functions of azimuth with the help of pre-existing processing flows. The so acquired data is fitted with π-periodic sinusoidal curves in order to obtain the anisotropic data coefficients in terms of the Fourier parameters a_C, a_S and b_C, b_S for surface and body waves, respectively.
With the acquired data, I will carry out the inversions for the anisotropic elastic coefficients G_C and G_S beneath each grid position separately. Thereafter, I will show the results of all positions for various layers.

5-3 Body wave inversion

The inversion is performed in analogy to the inversion on the 1D-model above. Each grid point is inverted separately. The results can be seen in Figure 5-6, which displays the orientation of the fast axis and the magnitude of the anisotropy of both the true model and the inversion results for the four deepest layers in the overburden. The near-surface layers are not shown as they are not meaningful due to the lack of SI-measurements, similar as it can be observed in the case of the layer between horizons H3 to H4. For this layer, the results are not constrained by data and hence deviate strongly from the true anisotropy. Looking at the other layers, a general agreement is visible. The overall strength of anisotropy, shown as the relative anisotropy G/L, is of the same order of magnitude. Regional deviations and slightly higher values can be observed in the inversion results. However, the lateral variations of the delay time between fast and slow signal are in the magnitude of 1 ms and appear to be too small to be measured accurately. On the other hand, the results for the orientation of the fast axis fits the true model in a very good manner, so that all characteristic features can be recognized. On closer inspection, a systematic deviation is visible in case of the layer between H4 and H5 in form of the signature of the near-surface anisotropy (e.g. the increased northern alignment in the lower left corner). As the SI measurements are solely available at the horizons H5, H6, and H7, information of the near-surface is missing, which in turn biases the inversion results. This is similar to the observations in case of the 1D-model and we expect that the inclusion of surface wave data improves the results, especially for the zone between H4 and H5.

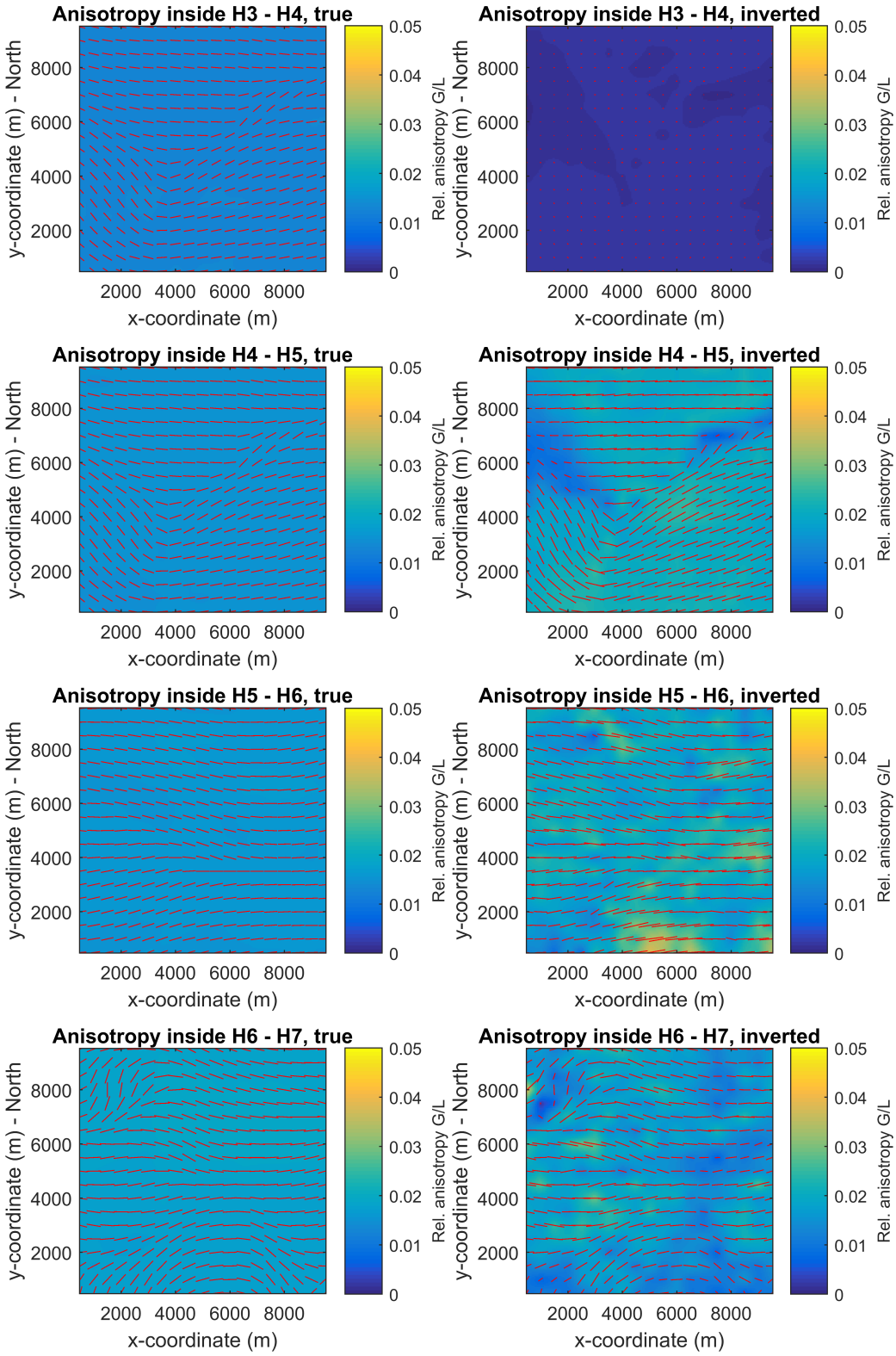

Figure 5-6: Relative anisotropy G/L (background) and fast axes direction Ψ_f (red lines) of the true model (*left column*) and from the body wave inversion (*right column*) for the 4 deepest overburden layers betweens horizons H3-H4, H4-H5, H5-H6, and H6-H7.

5-4 Surface wave inversion

This section presents the results obtained by inverting the surface wave data for the shallow 4 layers down to horizon H4. Figure 5-7 compares the theoretical anisotropy parameters with the results of the surface wave inversion. Eye-catching are the distorted corners in the graphs of the inversion results. The distortions are related to the incomplete data coverage over the azimuth. This applies to the values at the edges in general, which is why we will focus on the inner areas in the following discussion.

In terms of the anisotropy orientation, the inversion is able to resolve the characteristic structure of the near-surface. Interestingly, the fourth layer (H3-H4), which does not comprise the same anisotropy parameters as the near-surface by definition, exhibits similar anisotropy structures as the layers above. This results from the smoothing constraints in the inversion which relates neighboring layers to each other.

Unfortunately, the anisotropy amplitude is not fully recovered, even though characteristic patterns can be recognized. I assume that this results from the lateral S-wave velocity changes of the model which interfere with the measurement of the π-periodic varying phase velocities. This conforms to Eq. (2-7), in which the isotropic lateral velocity variation a_0 perturbs the surface wave phase velocity. Figure 5-8 gives an example, in which this effect occurs in an extreme manner. Displayed on the left hand side is an extracted region of the model, showing the S-wave velocity distribution and the fast axes directions. From a central point of view, not only the anisotropy but also the lateral velocity distribution follow a π-periodic azimuthal variation. The azimuthal variation of the lateral velocity distribution is just opposite to the variation of the anisotropy and is extinguishing its effect. This becomes clear when looking at inversion results, displayed on the right hand side of the figure. The resulting fast axes direction is contradicting the expected orientation due to the strong influence of the lateral velocity distribution. In practice, we would have to extract the effect of the laterally changing velocity before measuring the azimuthally varying surface phase velocities. However, this processing step is not feasible within the time frame of this thesis. For the following joint inversion, I will hence use the measured surface wave data *talis qualis* and will additionally carry out a joint inversion with the theoretically expected surface wave data.

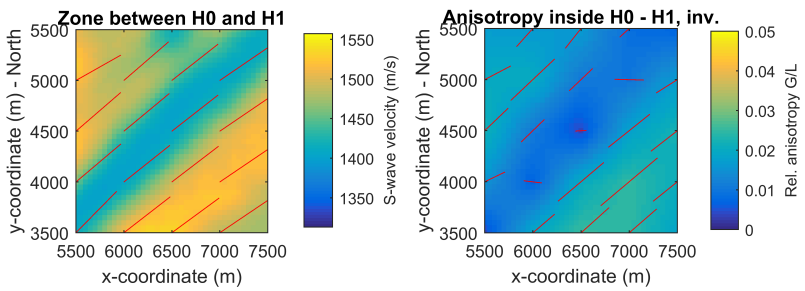

Figure 5-8: *Left:* S-wave velocity distribution and fast axes direction. *Right:* Inversion results (anisotropy magnitude and orientation) for the same region.

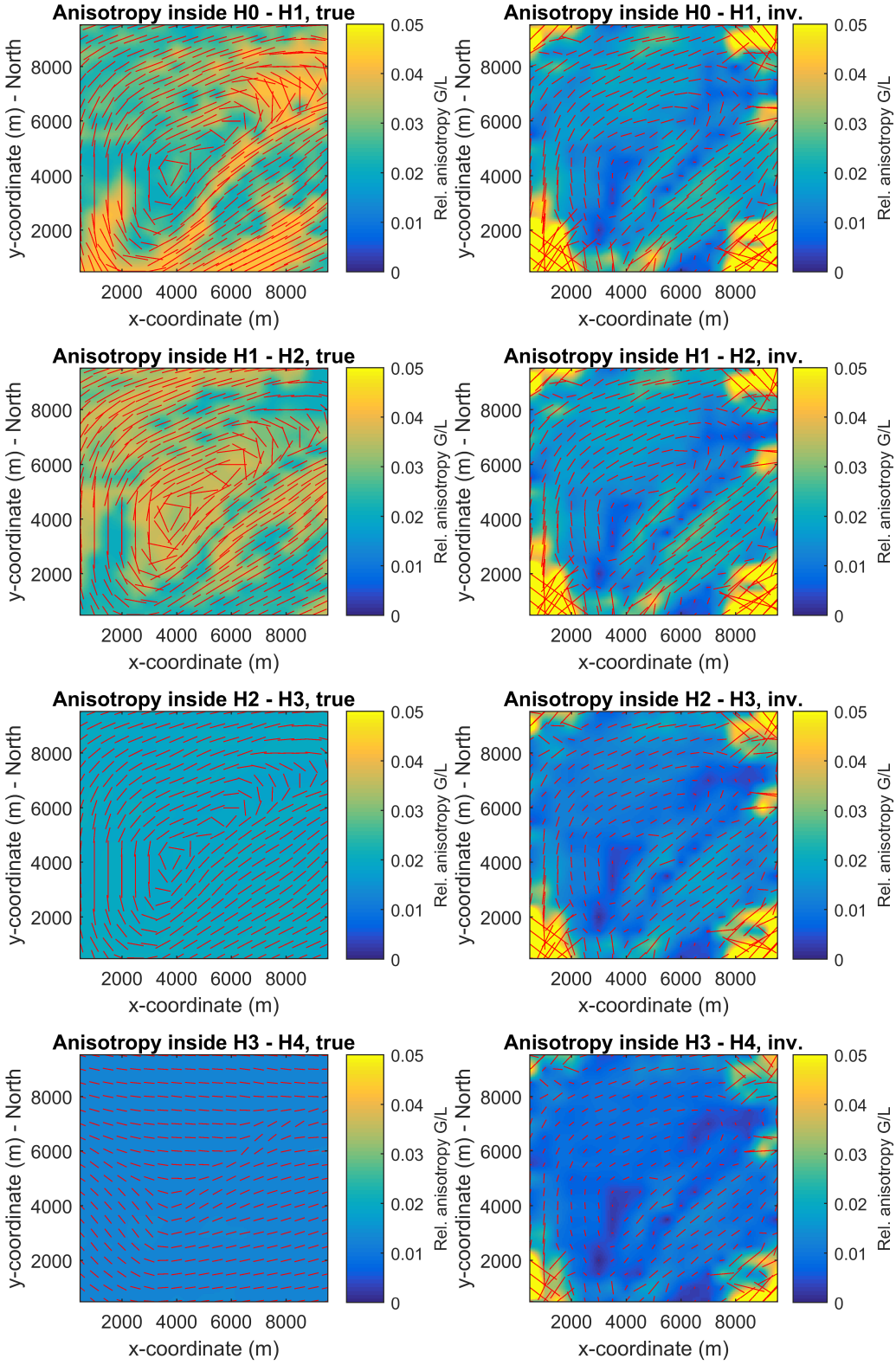

Figure 5-7: Relative anisotropy G/L (background) and fast axes direction Ψ_f (red lines) of the true model (*left column*) and from the surface wave inversion (*right column*) for the 4 shallow layer down to horizon H4.

5-5 Results joint inversion

This section presents the results from the joint inversions and compares them to the true anisotropy as well as to the results from the body wave inversion. First of all we evaluate the results for the layer between horizons H4 and H5, which are displayed in Figure 5-9. Remember that H5 is the horizon with the first SI measurement, which is why we expect here the strongest improvements when incorporating the information from the surface waves (apart from the improvements in the shallower layers for which no body wave data exists). The results with the incorporated measured surface wave data, which is biased by the laterally changing velocity distribution as discussed in the previous section, inherits the distortions at the corners due to the incomplete azimuth coverage in the surface wave measurement. Nevertheless, despite the influence of the laterally varying velocity distribution we can register improvements in the alignment of the fast axes direction compared to the result from the body wave inversion. Through the inclusion of the surface wave data, reduce the imprint of the near-surface anisotropy structure is reduced, which is for instance visible in the lower left corner of the graphs. The joint inversion using surface wave data directly derived from the model (denoted in the Figure 5-9 as syn. (synthetic)) further improves the result, so that it looks almost identical to the true anisotropy.

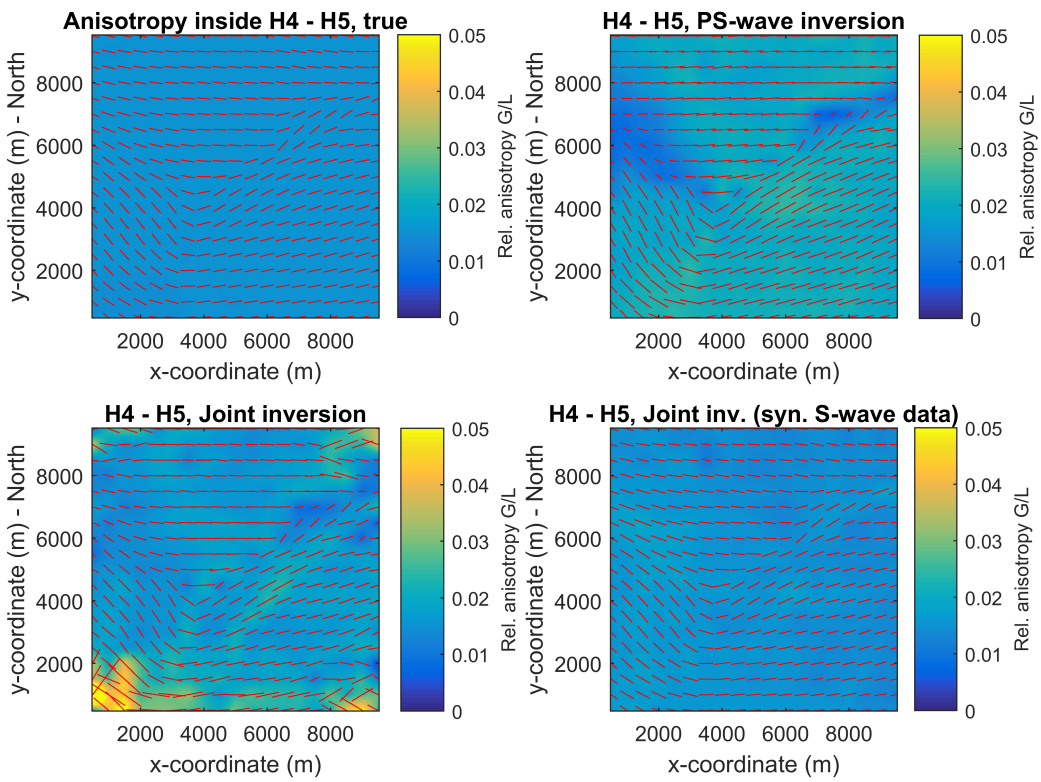

Figure 5-9: Relative anisotropy G/L (background) and fast axes direction Ψ_f (red lines) of the true model (*top left*) and from the body wave (PS-) inversion (*top right*), the joint inversion with measured surface wave data (*bottom left*) and the joint inversion with synthetic surface wave data (*top right*) for layer between horizons H4 and H5.

Next, for the two deepest layers from H5 to H6 and from H6 to H7, we do not expect remarkable improvements from the joint inversion as the SI measurement are taken relatively to the previous horizon and the surface waves do not penetrate that deep anyway. The corresponding results are shown in Appendix A-2 in Figure A-1 for completeness. As expected, there are no distinct changes visible between the results from the body-wave inversion and the results from the joint inversions.
Finally we evaluate the results of the layer between H3 and H4 which are displayed in Figure 5-10. This layer is located directly below the near-surface zone and contains the same anisotropic properties as the layer between H4 and H5. The body wave inversion was not able to determine its anisotropy due to the absent SI data. Including the information from the surface waves clearly improves the result as expected.

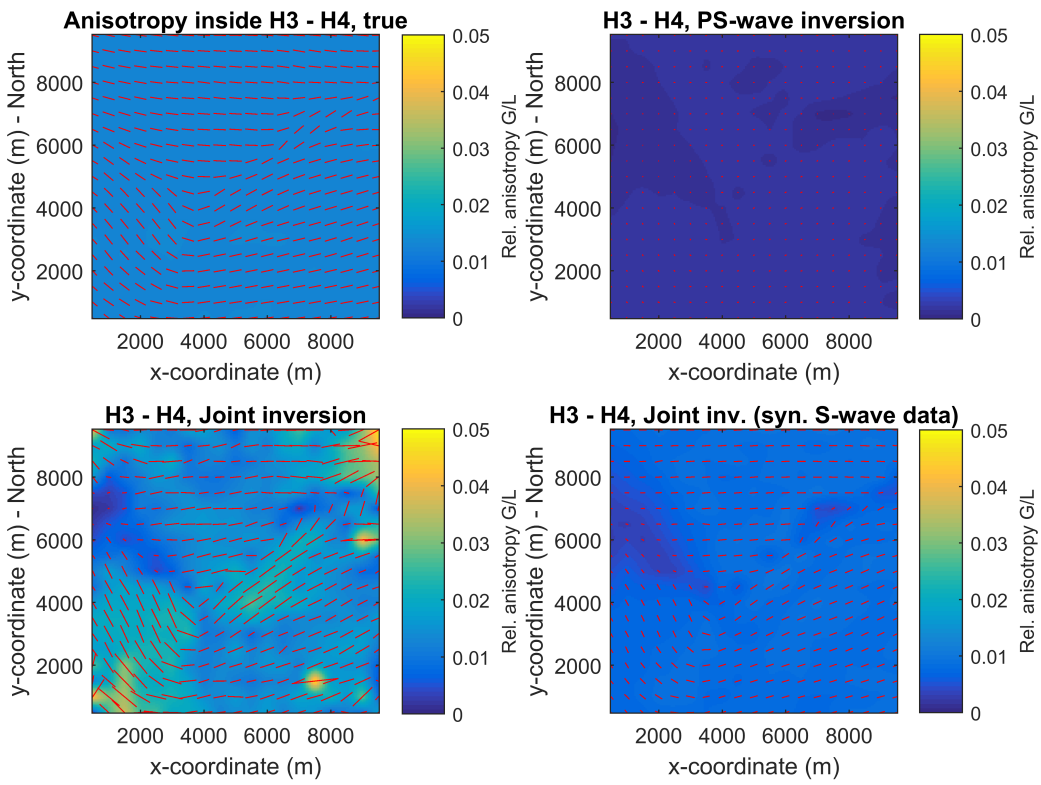

Figure 5-10: Relative anisotropy G/L (background) and fast axes direction Ψ_f (red lines) of the true model (*top left*) and from the body wave (PS-) inversion (*top right*), the joint inversion with measured surface wave data (*bottom left*) and the joint inversion with synthetic surface wave data (*top right*) for layer between horizons H3 and H4.

More interesting here is the comparison of the joint inversion results with the results from the sole surface wave inversion which is shown in Figure 5-11. Note that the same surface wave data is used for the two inversions. While the result from the sole surface wave inversion inherits a strong signature from the near-surface due to smoothing constraints as discussed in the section above, the result from the joint inversion fits much better the true anisotropy properties. This highlights that, in case surface wave data and body wave data contain information on the same anisotropy layers, the joint inversion combines the data of the two waves types in a complementary manner which improves both inversion types. This benefit of

the joint inversion was not visible in the 1D-model as the result of the surface wave inversion for the overlapping data zone had already been in good agreement with the true model.

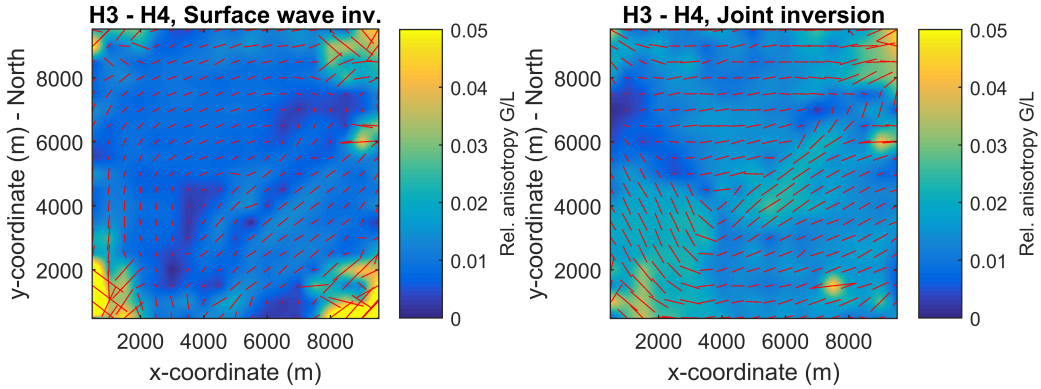

Figure 5-11: Relative anisotropy G/L (background) and fast axes direction Ψ_f (red lines) from the surface wave inversion (*left*) and, from the same surface wave data, the joint inversion (*right*) for layer between horizons H3 and H4.

Chapter 6

Conclusion and Outlook

In this thesis I investigated shear-wave velocity anisotropy and its related phenomenon of shear-wave splitting (SWS). I presented an approach to jointly invert data from surface waves and body waves in order to determine the corresponding anisotropic subsurface properties. The inversion results of the synthetic data examples demonstrate the complementarity of the two wave types and the benefits of a joint inversion.

6-1 Summary and conclusion

In reflection seismology, shear-wave velocity anisotropy can be detected and analyzed with the help of PS-waves. However, PS-waves can not be consulted for near-surface anisotropy. As a consequence, shear-wave splitting (SWS) measurements are potentially being flawed which leads to an incomplete compensation when correcting the seismic image for the splitting effect. In order to ascertain near-surface anisotropy and hence fill the lack of information, surface wave phase velocity was investigated in the present study.
After establishing the theory, which relates the anisotropic elastic coefficients of the subsurface to the anisotropic coefficients from surface wave data and body wave data, respectively, I showed how the two systems of different wave types can elegantly be combined into one scheme. The neat point here is that both surface waves and body waves are sensitive to the same subsurface anisotropic properties.
Subsequently I suggested two normalization approaches to prepare the joint system for the inversion. The normalization is important to enable an holistic regularization as the data inputs from surface waves and body waves are of different magnitude and dimension.
In order to test the performance of the joint inversion in retrieving the subsurface velocity anisotropy compared to the performance of a sole body wave inversion, I prepared a 1D-model and a more complex 3D-model using the SEAM 'Barret Unconventional Model' as a reference. S-wave anisotropy was introduced throughout the whole depth. The anisotropy in the 3D-model was adopted in a geologically meaningful way what qualifies the model for future anisotropy studies.

In the analysis of seismic data, limitations had to be set on the signal bandwidth. The here employed method for the body wave analysis assumes large wave signal periods in respect to the delay time δt between fast and slow traveling wave, which is why a low-pass filter up to 8 Hz was applied. This led to the overlapping of reflected waves from closely spaced horizons, which resulted later in an incomplete recovery of the anisotropy magnitude. For the surface wave analysis, the finite receiver spread results in a limited wavenumber resolution. It has been observed, that this leads to a poorer velocity resolution for surface waves of lower frequencies which can harm the determination of the anisotropy properties. In the case of a near-surface with constant anisotropy, where the increased penetration depth of low frequency waves it not necessary to identify the anisotropy of deeper layers, it can hence be advisable to rely on higher frequency surface waves.
The inversion results demonstrate the value of combining surface waves and body waves. In the case of the 1D-model, the determination of the anisotropy in the near-surface zone is improved strongly through the incorporation of the surface waves. To highlight this, I corrected the seismic data for the shear-wave splitting effect using the inversion results. While the compensation with the results from the body wave inversion reveal deficiencies, the results from the joint inversion achieve almost complete compensation thanks to the additional information for the shallow layers.
The inversions for the 3D-model were carried out successively on each surface grid position. Despite this 1D-nature of the inversion, the inversion results exhibit a smooth lateral coherency. While the anisotropy orientations could generally be well determined, lateral changes of the anisotropy magnitude were, especially in greater depths, too small to be measured accurately. The inversion results from the surface waves revealed incompleteness in the data analysis. Here, the lateral isotropic velocity variations contaminate the azimuthal phase velocity measurements. As a consequence, the inverted anisotropic properties deviate in some regions strongly from the true model parameters. This concerns mainly the anisotropy magnitude, even though flaws in the recovery of the principal directions were also observed locally. Nonetheless, the incorporation of the measured surface wave data resulted in improvements of the anisotropy determination in the layer below the near-surface. To demonstrate the benefits from the inclusion of surface waves, I additionally carried out a joint inversion using theoretical surface wave data without perturbation from the lateral changing isotropic velocity. The inversion results showed that the layer below the near surface could be freed from the influence of the shallow anisotropy and is consequently in good agreement with the true model in terms of S-wave velocity anisotropy properties. Vice versa we observed, that the informations from the body waves can constrain flawed surface wave data if the data of the two wave types are overlapping over the same region. This underlines that the joint inversion is combining surface waves and body waves in an complementary way.

6-2 Outlook

In the following I want to give suggestions for future elaboration on the joint inversion for shear-wave velocity anisotropy from surface and body waves.
In this thesis I have used Fourier coefficients to describe the azimuthally varying anisotropic properties. Subsequently, I have established a system corresponding to the cosine-term and one corresponding to the sine-term. The two systems which relate the subsurface anisotropic elastic properties to the seismic wave anisotropic behaviors are inverted independently. As the

data inputs for cosine-term and sine-term can vary significantly in magnitude, the independent inversions are likely to perform differently which influences the ratio of the Fourier coefficients. Alternatively to the Fourier coefficients, the two systems could be rewritten in terms of an amplitude and a phase shift. The inversions would then directly aim for the anisotropy magnitude and its orientation, respectively. This is potentially beneficial in case *a priori* information constrain either anisotropy magnitude or angle, as those can then be regularized independently.

Next, it has been realized, that the lateral isotropic S-wave velocity variation can strongly influence the measurement of the π-periodic surface wave phase velocity azimuthal variation. The biased surface wave data consequently degrade the performance of the joint inversion. Therefore, the extraction of the lateral isotropic variation must be introduced as a standard processing step before analyzing the surface wave phase velocity.

Further, the inversion on the 3D-model was carried out successively in a 1D-manner for each position. To improve the inversion results, a 3D-inversion should be implemented which allows lateral regularization. By this, subsurface characteristics and *a priori* information could better be taken into account.

Finally, once the above suggestions have been addressed, the established joint inversion of surface and body wave can be used on real data. Even though the above created 3D-model is supposed to resemble the real subsurface, the synthetic data are not contaminated with noise which will certainly influence the data analysis and the inversion results.

Bibliography

Boiero, D. and Bagaini, C. (2016). Horizon-based splitting intensity analysis and inversion for anisotropic characterization. In *78th EAGE Conference and Exhibition 2016*.

Chevrot, S. (2000). Multichannel analysis of shear wave splitting. *Journal of Geophysical Research: Solid Earth*, 105(B9):21579–21590.

Crampin, S. (1981). A review of wave motion in anisotropic and cracked elastic-media. *Wave motion*, 3(4):343–391.

Crampin, S. (2006). The new geophysics: a new understanding of fluid-rock deformation. In *Eurock*, pages 539–544.

Crampin, S., Chesnokov, E. M., and Hipkin, R. A. (1984). Seismic anisotropy-the state of the art. *First Break*, 2(3):9–18.

Crampin, S. and Gao, Y. (2009). A review of a quarter century of international workshops on seismic anisotropy in the crust (0iwsa–12iwsa). *Journal of seismology*, 13(2):181–208.

Hering, A., Misiek, R., Gyulai, A., Ormos, T., Dobróka, M., and Dresen, L. (1995). A joint inversion algorithm to process geoelectric and sutface wave seismic data. part i: basic ideas1. *Geophysical Prospecting*, 43(2):135–156.

Kennett, B. (2009). *Seismic wave propagation in stratified media*. ANU Press.

Lisitsa, V. and Vishnevskiy, D. (2010). Lebedev scheme for the numerical simulation of wave propagation in 3d anisotropic elasticity. *Geophysical Prospecting*, 58(4):619–635.

Mallick, S. and Frazer, L. N. (1990). Computation of synthetic seismograms for stratified azimuthally anisotropic media. *Journal of Geophysical Research: Solid Earth*, 95(B6):8513–8526.

Manukyan, E., Latzel, S., Maurer, H., Marelli, S., and Greenhalgh, S. A. (2012). Exploitation of data-information content in elastic-waveform inversions. *Geophysics*, 77(2):R105–R115.

Montagner, J.-P., Griot-Pommera, D.-A., and Lavé, J. (2000). How to relate body wave and surface wave anisotropy? *Journal of Geophysical Research: Solid Earth*, 105(B8):19015–19027.

Montagner, J.-P. and Nataf, H.-C. (1986). A simple method for inverting the azimuthal anisotropy of surface waves. *Journal of Geophysical Research: Solid Earth*, 91(B1):511–520.

Oristaglio, M. (2014). Seam update. *The Leading Edge*, 33(4):380–382.

Rand, O. and Rovenski, V. (2007). *Analytical methods in anisotropic elasticity: with symbolic computational tools*. Springer Science & Business Media.

Sieminski, A., Paulssen, H., Trampert, J., and Tromp, J. (2008). Finite-frequency sks splitting: measurement and sensitivity kernels. *Bulletin of the Seismological Society of America*, 98(4):1797–1810.

Silver, P. G. and Chan, W. W. (1991). Shear wave splitting and subcontinental mantle deformation. *Journal of Geophysical Research: Solid Earth*, 96(B10):16429–16454.

Smith, M. L. and Dahlen, F. A. (1973). The azimuthal dependence of love and rayleigh wave propagation in a slightly anisotropic medium. *Journal of Geophysical Research*, 78(17):3321–3333.

Thomsen, L. (1986). Weak elastic anisotropy. *Geophysics*, 51(10):1954–1966.

Wikipedia (2016). Isotropy — wikipedia, the free encyclopedia. [Online; accessed 30-July-2016].

Appendix A

Parameters and further results

A-1 1D-model: Set-up parametrization

Before displaying the model parameters it is necessary to introduce the so-called *Thomsen* parameters (Thomsen, 1986), which are convenient to describe an anisotropic material:

$$\epsilon = \frac{C_{11} - C_{33}}{2C_{33}}, \tag{A-1}$$

$$\gamma = \frac{C_{66} - C_{44}}{2C_{44}}, \tag{A-2}$$

$$\delta = \frac{(C_{13} + C_{44})^2 - (C_{33} - C_{44})^2}{2C_{33}(C_{33} - C_{44})}. \tag{A-3}$$

Given the background P-wave and S-wave velocities v_p and v_s, respectively, which correspond in an HTI medium to the fast axis, and using the relations in Eq. (2-3), the elastic coefficients of the stiffness matrix for the HTI medium can successively be inferred with the given *Thomsen* parameters:

$$\begin{aligned}
C_{33} &= \rho v_p^2, \\
C_{22} &= C_{33}, \\
C_{11} &= C_{33}(2\epsilon + 1), \\
C_{44} &= \rho v_s^2, \\
C_{66} &= C_{44}(2\gamma + 1), \\
C_{55} &= C_{66}, \\
C_{13} &= \sqrt{\delta(2C_{33}(C_{33} - C_{44})) + (C_{33} - C_{44})^2} - (C_{44}).
\end{aligned} \tag{A-4}$$

From here, all directional velocities can be calculated with the relations in Eq. (2-3). Table A-1 displays all necessary parameters to set up the 1D-model.

Table A-1: Set-up parameters for the 1D-model: Layer number, layer thickness d, background P-wave velocity v_p, background S-wave velocity v_s, density ρ, and dimensionless *Thomsen* parameters ϵ, γ, and δ.

Layer	d (m)	v_p (m/s)	v_s (m/s)	ρ (l/kg)	ϵ	γ	δ
1	50	2325	1360	2.120	-0.0078	-0.0390	0.0079
2	50	2450	1700	2.225	-0.0089	-0.0370	0.0086
3	50	2550	1260	2.175	-0.0096	-0.0408	0.0092
4	150	3000	1520	2.200	-0.0110	-0.0420	0.0105
5	650	3100	1840	2.240	-0.0180	-0.0205	0.0170
6	550	3175	1900	2.645	-0.0252	-0.0158	0.0234
7	500	3300	1940	2.500	-0.0347	-0.0128	0.0319
8	450	3575	1980	2.650	-0.0430	-0.0134	0.0396
9	50	4600	2700	2.350	-0.0473	-0.0183	0.0442
10	150	3625	2350	2.520	-0.0493	-0.0201	0.0455
11	450	5775	3230	2.650	-0.0546	-0.0215	0.0507
12	150	3700	2300	2.460	-0.0599	-0.0226	0.0553
13	500	6200	3360	2.645	-0.0654	-0.0235	0.0611
14	750	5875	3180	2.350	-0.0700	-0.0240	0.0650

A-2 3D-model: Results joint inversion

Figure A-1 shows the true model anisotropy and results from body wave and joint inversion for the 2 deepest layers between horizons H5 to H6 (*top*) and H6 to H7 (*bottom*). As the surface waves are not sensitive in the corresponding depths, the joint inversion does not improve the results of the body wave inversion.

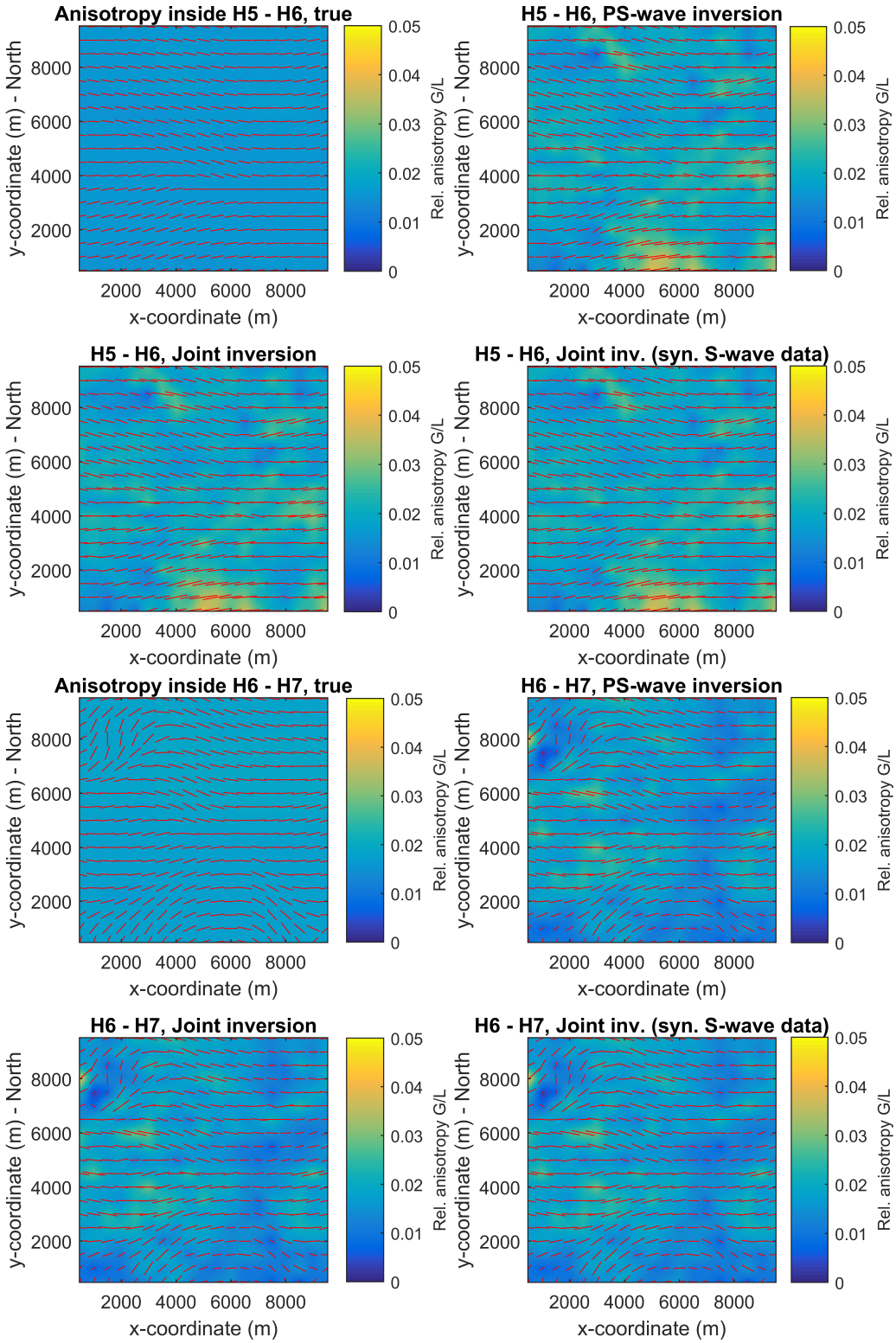

Figure A-1: Relative anisotropy G/L (background) and fast axes direction Ψ_f (red lines) of the true model (*top left*) and from the body wave (PS-) inversion (*top right*), the joint inversion with measured surface wave data (*bottom left*) and the joint inversion with synthetic surface wave data (*top right*) for layer between horizons H6 - H7 (*top half*) and H6 - H7 (*bottom half*).